Scatter artifact correction in cone-beam CT images

Peter G. F. Watson
Medical Physics Unit
McGill University
Montréal, Québec
Canada

A Thesis submitted to the
Faculty of Graduate Studies and Research
in partial fulfillment of the requirements for the degree of
Master of Science in Medical Radiation Physics

For Lorri.

Contents

List of Figures

List of Tables

Abstract

Cone-beam computed tomography (CBCT) images suffer from poor image quality, in a large part due to scattered x-rays. In this work, a fast and accurate Monte Carlo based scatter correction algorithm was implemented on real CBCT data. A fast Monte Carlo simulation developed in the EGSnrc framework was used to transport photons through an uncorrected CBCT scan. From the simulation output, the contribution from both primary and scattered photons for each projection image was estimated. Using these estimates, a subtractive scatter correction was performed on the CBCT projection data. Implementation of the scatter correction algorithm on CBCT phantom scans was shown to help mitigate scatter-induced artifacts, such as cupping and streaking. The scatter corrected images were also shown to have improved accuracy in reconstructed attenuation coefficient values. These results suggest that the proposed scatter correction algorithm is successful in improving image quality in real CBCT images, are promising results towards the reliable use of CBCT images in adaptive radiotherapy.

Abrégé

Les images de tomodensitométrie à faisceau conique (CBCT) souffrent d'une qualité d'image inférieure en partie due aux rayonnement diffusés. Dans cet ouvrage, un algorithme Monte Carlo rapide et précis fut appliqué sur des images CBCT cliniques. En utilisant un logiciel de transport de particules à base Monte Carlo pour transporter des photons dans un CBCT où les données n'ont pas été corrigés, la contribution des photons diffusés primaires et secondaires pour chaque image fut estimée. En utilisant cet estimé, une correction fut apportée sur les données du CBCT. La méthode de correction CBCT a démontré sa capacité de mitiger les artéfacts introduient par la diffusion des photons. Les images corrigées ont montré une plus grande précision pour la reconstruction des coéfficients d'atténuation. Ces résultats suggèrent que la méthode proposée pour corriger des images CBCT fut un succès pour l'amélioration de la qualité d'images CBCT réelles, et insinuent une utilisation fiable des images CBCT en radiothérapie adaptative.

Acknowledgments

I would like to thank everyone who supported and assisted me over the past two years. Many times I found myself asking, "a second M.Sc. degree? *Really?*". There were some days where I was less than motivated, but thanks to my friends and family, I persevered. Special thanks goes to my supervisor, Dr. Jan Seuntjens, for proposing the research project and providing his expertise. Dr. Ernesto Mainegra-Hing must be thanked for providing me with his software, and answering my many questions about them. Dr. Emilie Soisson was integral in performing the CBCT scans presented in this work, and also in acquiring the raw CBCT projection data. Fruitful discussions on imaging systems and image quality were provided by Dr. Issam El-Naqa. I must also thank Dr. Glenn Wells of the Ottawa Heart Institute for allowing me to use his C implementation of the FDK reconstruction algorithm. Questions pertaining to Varian OBI CBCT raw data were graciously answered by Dr. Peter Munro of Varian Medical Systems. Fan-beam CT images were provided by Amanda Dyess (ACR Accreditation phantom), and Desmond Milroy (RANDO head phantom). Marc–Andre Renaud and Piotr Pater both assisted in translating the abstract into french.

I cannot forget to mention the social support of my colleagues in the Medical Physics Unit, who made coming in to work a more enjoyable experience. Their commiseration during the coursework portion of the M.Sc. was appreciated. Thanks to Dr. Ervin Podgorsak for teaching me to deal with fear.

Most of all, I must thank my wife, Lorri-Anne Watson, for putting up with my near-eternal studenthood. For all intents and purposes, she was a single mother while I was taking courses, and her sacrifice for my education must be acknowledged. Thanks to my son, Petey, for making all this hard work seem meaningful.

Scatter artifact correction in cone-beam CT images

1

Introduction

1.1 Cancer and Radiation Therapy

Cancer, the unregulated growth and spread of abnormal cells, is one of the leading causes of death worldwide [1], and the leading cause of death in Canada [2]. In 2012, it is estimated that 186 400 new cases of cancer and 75 700 deaths will occur in Canada alone [2]. For the treatment of cancer, there are three common treatment methods; surgery (removal of cancerous tissue), chemotherapy (cancer-killing pharmaceuticals), and radiation therapy (cancer-killing radiation). These treatment options can be used on their own, but are often prescribed in combination with each other.

Radiation therapy, or radiotherapy, uses ionizing radiation to treat malignant disease by depositing energy in cancerous cells, while sparing surrounding healthy tissue. The absorbed dose, D, defined as the energy E absorbed per unit mass m

$$D = \frac{dE}{dm}, \tag{1.1}$$

is a quantity which is correlated to the biological response of irradiated tissue. The goal of radiotherapy is to then deliver a lethal dose of radiation to the tumour, while minimally irradiating nearby healthy organs and tissues. The most common form of radiotherapy is known as *external beam radiation therapy*, where a radiation source (i.e. linear accelerator) external to the patient is used to irradiate the tumour. Less commonly, the radiation source can be inserted or placed in close proximity to the tumour, in a modality known as *brachytherapy*.

1.1.1 Radiotherapy Treatment Planning

The process of delivering a high dose with external beam radiation therapy to a defined target volume while minimizing dose to healthy tissue must be carefully planned and optimised. This process begins first with patient diagnosis, then localisation of the target. A number of three-dimensional imaging modalities can be used for this purpose, such as computed tomography (CT), positron-emission tomography (PET), single photon emission computed tomography (SPECT), ultrasound (US), and magnetic resonance imaging (MRI). Currently, CT is the standard imaging technique for radiotherapy treatment planning.

First, the patient is scanned in a CT simulator, positioned as they would be during actual treatment. The patient positioning during CT simulation is referenced to a set of small radio-opaque ball bearings (bbs) placed on the patient's skin before scanning. The patient is then localised in the CT scanner by aligning the bbs with the CT simulator's localization lasers. These bb markers act as reference coordinates to properly position the patient during radiation therapy. From the treatment planning CT images, target volumes are contoured and organs at risk (OAR) are delineated. Surrounding the tumour target volume, margins are added to include any microscopic disease and to account for patient positioning errors and patient motion during treatment. This larger volume is known as the planning target volume (PTV), and is considered to be the target that needs to be irradiated with a lethal dose.

Radiation beams are then chosen which adequately cover the PTV and limit dose to the OAR. This step is typically performed by software known as a treatment planning system (TPS), which employs dose calculation algorithms to calculate dose distributions according to the beam radiation types and arrangement. Using techniques such as intensity modulated radiation therapy (IMRT), it is possible to deliver a highly conformal dose to the target volume while avoiding critical structures. Associated with this conformal coverage is a steep dose gradient outside of the PTV. This rapid fall-off of dose requires accurate delineation of the target during treatment planning and accurate localisation of the target during treatment to ensure the malignancy is

not under-dosed.

1.2 Towards Adaptive Radiotherapy

1.2.1 Image Guided Radiotherapy

Image guided radiation therapy (IGRT) refers to emerging techniques in treatment planning, patient setup, and radiation delivery that rely on imaging information for target definition, patient immobilisation, and delivery guiding tools [3]. The goal of IGRT is to help minimise the PTV margins by reducing the uncertainty in tumour target localisation, and to deliver the prescribed dose distribution as accurately as possible. It has been shown that non-optimal PTV margins can adversely affect treatment outcomes [4].

Early examples of IGRT used two-dimensional imaging systems (i.e. ultrasound and electronic portal imaging) for guidance, with limited success. IGRT was extended with the introduction of three-dimensional, volumetric imaging systems incorporated into the radiotherapy treatment room. Examples of these are three-dimensional ultrasound, and computed tomography (CT) on rails [5]. CT on rails involves installing a diagnostic quality CT scanner in the treatment room, with its own isocenter. This system relies on the assumption of mechanical stability between the CT scanner and linear accelerator [3].

1.2.2 CBCT in IGRT

A more practical advancement of 3D IGRT is the use of cone-beam computed tomography (CBCT) in the clinic. By integrating a CBCT system into a medical linear accelerator, it is possible to acquire a volumetric image of the patient in their treatment position. Using the treatment beam and electronic portal imager, megavoltage (MV) CBCT IGRT has been investigated, however these images suffer from poor signal-to-noise and soft-tissue contrast [6]. Better image quality can be obtained from a kilovoltage (kV) CBCT system, mounted on the linear accelerator gantry [7, 8]. Currently, kV CBCT is used routinely in the clinic to correct for patient setup errors.

Furthermore, it has been shown that head and neck cancer patients undergoing daily IGRT with kV CBCT lead to a reduction of PTV margins [9].

1.2.3 Adaptive Radiotherapy

In the conventional radiotherapy treatment planning procedure outlined in Section 1.1.1, the treatment plan retrieved from the TPS is based on the patient's initial planning CT scan. A typical course of radiation therapy can last over 8 weeks, during which time the patient may lose weight, organs may experience deformation, and the tumour itself may change shape, size, and position. These anatomical changes are not reflected in the treatment plan, which can lead to systematic errors in dose delivery [10].

Ideally, the treatment plan would be periodically re-optimised to take into account these anatomical changes. This process of re-optimisation is known as *adaptive radiotherapy*, or ART. In the framework of on-line ART, treatment planning workflow would follow a "scan, plan, and treat" scheme, where up-to-date imaging information would be used to replan the patient immediately prior to treatment. One possible ART approach would be to use the daily CBCT image to create the adapted treatment plan. For this approach to be feasible, it would be necessary to be able to accurately delineate target volumes and perform dose calculations on CBCT images.

The current imaging standard for radiotherapy planning is conventional, fan-beam CT (FBCT) [11], which has been dosimetrically validated [12]. Unfortunately, CBCT images have inferior image quality compared to FBCT, in a large part due to scattered x-ray artifacts (see Figure 1.1) [13]. The feasibilty of using CBCT images for organ contouring and dose calculations has been investigated [14, 15, 16, 17]. The differences between FBCT and CBCT-based dose calculations vary between <1% to 3% [15], and in some complex cases up to 10% [17], depending on the phantom or patient site studied. In contouring soft tissue boundaries, the poor contrast of CBCT images leads to larger inter-observer contour variations than FBCT [14]. Before CBCT-based ART can be fully realised, CBCT image quality must be improved.

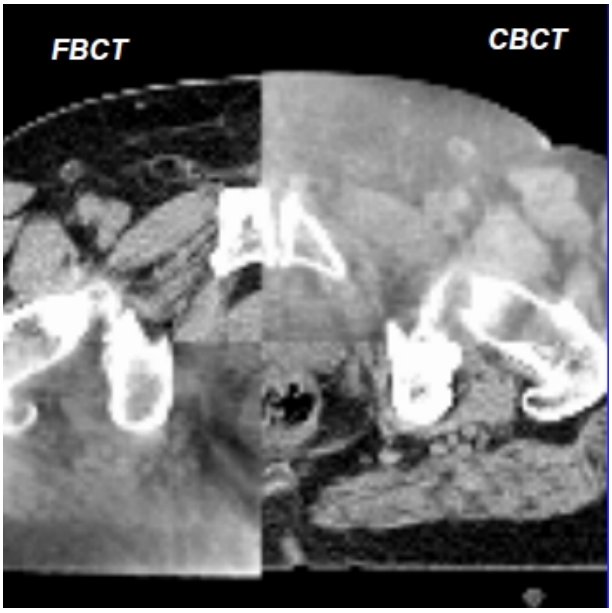

Figure 1.1: Comparison of image quality between fan-beam CT (FBCT) and cone-beam CT (CBCT) for a pelvis scan. Note the noise and poor soft tissue contrast of CBCT.

1.3 Thesis Outline

The proposed work consists of implementing a scatter correction for real CBCT images, in order to improve their image quality. To do so, a fast Monte Carlo simulation will be used to estimate the contribution from primary and scattered photons for each projection image. From these simulated projections, a scatter correction will be applied to real CBCT projection data, which will then be reconstructed. In order to assess the performance of the scatter correction, the results will be compared with "clinical ground truth" FBCT images.

Chapter 2 is an primer to computed tomography, with a focus on CBCT reconstruction, and scatter mitigation strategies. In Chapter 3, the Monte Carlo simulation of photon transport is discussed, as well as the CBCT scanner and phantoms used in this study. Chapter 4 outlines the steps of the proposed scatter correction algorithm in detail. Results of the project are shown and discussed in Chapter 5, and Chapter 6 contains conclusions and comments on future work.

2

Basics of Cone Beam Computed Tomography

2.1 Introduction to Computed Tomography

Computed tomography (CT) is an imaging modality where x-ray projection radiographs from multiple view angles are used to reconstruct a three dimensional volume. In clinical applications, CT allows for non-invasive imaging of the interior of a patient. An invaluable tool in medical imaging, the CT scanner was invented by Godfrey Hounsfield and Allan Cormack, earning them the Nobel Prize for Medicine in 1979. Preceding this invention, the mathematical principles behind CT had been developed by J. Radon in 1917 [18]. In radiation therapy, CT images are the standard for patient treatment planning and dose calculation.

A conventional CT scanner uses a narrow fan-beam geometry, effectively producing one-dimensional transmission measurements through an object of interest. CT reconstruction from these measurements yields a two-dimensional cross-sectional image, or "slice"[1]. In actuality, this two-dimensional image corresponds to a three-dimensional section of the object, with depth equal to the slice thickness of the x-ray fan-beam (typically between 1 to 10 mm). To image a larger volume, many axial CT slices are acquired sequentially along the longitudinal axis, and are combined, or "stacked" together.

[1]This slice is what gives us the word "tomography", which comes from the Greek *tomos* (slice) and *graphein* (write).

2.1.1 CT Scanner Components

The main components of a CT scanner are the x-ray tube, collimator and filtration, compensator (or "bowtie" filter), detector, and reconstructor computer. The x-ray tubes used in CT scanners typically operate at voltages between 80 to 140 kVp with tube currents between 20 to 400 mA, and must be able to endure relatively long scan times (on the order of minutes). The CT slice thickness and field of view (FOV) are determined by collimators placed immediately downstream from the x-ray tube, which define the dimensions of the x-ray beam. The collimators placed parallel to the plane of rotation define the slice thickness, and the collimators orthogonal to the plane define the FOV. Beam quality is in part determined by filters installed at the exit window of the x-ray tube, which remove unwanted low energy photons[1] from the x-ray spectrum. A compensator is used to regulate the intensity uniformity at the detector by preferentially attenuating the beam along the lateral field periphery, while hardly reducing intensity at the field center. Compensators also help to reduce x-ray scatter in the patient, and act as an additional filter, further reducing patient dose. The CT detector is a device which measures the x-ray intensity transmitted through the patient. While there are a number of CT detector technologies (ex. ionisation chambers & solid state scintillators), they perform the same task of converting the incident x-ray intensity to a corresponding electronic signal, which is then digitised and sent to the reconstructor computer. It is the job of the reconstructor computer to preprocess the raw projection data, and then perform tomographic reconstruction on them. These reconstructed CT images are often stored in DICOM (Digital Imaging and Communications in Medicine) file format [19], and are transferred to a PACS (Picture Archiving and Communications System) which allows the images to be accessed from a computer network.

[1] Low energy photons (< 20 keV) increase the dose to the patient, without contributing to image quality

2.1.2 Image reconstruction

During a CT scan, each pixel of a CT detector measures a transmitted x-ray intensity, I_{t}. This transmitted intensity is related to the unattenuated intensity, I_0, along the same path from x-ray source to detector pixel by the Beer-Lambert law;

$$I_{\mathrm{t}} = I_0 e^{-\mu\ell} \tag{2.1}$$

where ℓ is the thickness of the patient along the ray connecting the source to detector, and μ is the average linear attenuation coefficient along the ray. Since μ values are related to material properties, such as density and atomic number, anatomical information can be extracted from a μ map of the patient. The goal of CT reconstruction is then to obtain a patient image of $\mu(x, y)$ values.

Most CT scanners use an x-ray tube as a photon source, which emits a polyenergetic photon spectrum of energies between 0 and $E_{\max}$. The transmitted intensity of Eq.(2.1) is then expressed as:

$$I_{\mathrm{t}} = \int_0^{E_{\max}} I_0(E) \cdot e^{-\int_0^{\ell} \mu(x,y)\mathrm{d}s} \mathrm{d}E. \tag{2.2}$$

After CT image acquisition, the raw intensity data is preprocessed to create what is known as a *sinogram*. Each point in the sinogram corresponds to the measured pixel intensity for a given projection angle, θ, and pixel position along the detector, d, and is defined as:

$$p(d, \theta) = -\ln \frac{I_{\mathrm{t}}}{I_0}. \tag{2.3}$$

From Eq.(2.2), the sinogram then represents the line integral of the energy-averaged $\mu(x, y)$, Radon transformed to (d, θ) coordinates. In the case of parallel projections, the sinogram can be written as

$$p(d, \theta) = \int_{-\infty}^{\infty} \int_{-\infty}^{\infty} \mu(x, y)\delta(y\cos\theta - x\sin\theta - d)\mathrm{d}x\mathrm{d}y \tag{2.4}$$

The sinogram is then input into a tomographic reconstruction algorithm which calculates the $\mu(x, y)$ distribution.

The most commonly used reconstruction algorithm is filtered backprojection (FBP), which (not surprisingly) involves filtering the projection data and backprojecting it

across the field of view. The filtered backprojection algorithm is discussed in more detail when describing cone-beam reconstruction in Section 2.4. While relatively computationally efficient, filtered backprojection algorithms have some drawbacks, such as poor handling of noisy or missing projection data. Another class of reconstruction algorithms, known as iterative methods, offer improvements over filtered backprojection as they can more realistically model the imaging system (i.e. include Poisson noise). A common iterative reconstruction technique is the maximum likelihood expectation maximization (MLEM) algorithm, which is often used in positron emission tomography (PET) and single-photon emission computed tomography (SPECT) [20]. Iterative reconstruction algorithms have not yet become popular in CT reconstruction due to lengthy computation times, however advances in graphics processing unit (GPU) parallelization techniques may lead to their clinical implementation [21].

2.1.3 CT-Based Treatment Planning

Once the patient μ matrix of voxels[1] has been reconstructed, each voxel μ value is converted to a CT number, or Hounsfield Unit (HU). The HU is defined by the following equation:

$$HU = 1000 \times \frac{\mu_i - \mu_{\text{water}}}{\mu_{\text{water}}} \tag{2.5}$$

where μ_i and μ_{water} are the attenuation coefficients of a given voxel i and water, respectively. One HU then represents a voxel μ difference of 0.1% from the μ of water for a given beam quality.

CT image HU values are of importance in radiation therapy planning as they are what provide the necessary image contrast to delineate and contour soft tissues, such as organs at risk and tumour volumes. HU values provide information about the average attenuation properties of the voxel medium, which can then be used to identify voxel mass density and material type. This conversion from HU to material type and mass density (ρ) is important for radiation dose calculations during treatment planning [12, 22, 23]. For accurate patient dose calculations (i.e. accounting for tissue

[1] A **voxel** (*volumetric pixel*) is a pixel which represents 3D image data.

inhomogeneities), the electron density (ρ_e) must be known for each voxel. Electon density, defined as the number of electrons per unit volume, is proportional to the mass density, atomic number (Z) and atomic mass number (A) of the material in question:

$$\rho_e = \rho \frac{Z}{A} N_A, \tag{2.6}$$

where N_A is the Avogadro number ($N_A = 6.022 \times 10^{23}$ mol^{-1}). Thomas et al. [24] reported that an 8% error in electron density would typically result in a 1% difference in calculated dose.

Unfortunately, for kilovoltage photon beams (such as those used in CT scanners), there is no direct relationship between μ and ρ_e. Photons in this energy range (40–120 keV) interact with tissue (effective atomic numbers between 5 and 14) through a combination of the photoelectric effect, incoherent (Compton) scatter and coherent (Rayleigh) scatter. While Compton scattering is essentially independent of Z, Rayleigh scattering and photoelectric effect exhibit a Z dependence. In the case of the photoelectric effect, the cross-section dependence on Z is quite large ($\sim Z^3$), thus the assignment of ρ to μ for a heterogeneous object is not straightforward.

The most common method for converting CT images to density maps is through an image value to density table (IVDT) calibration curve. This curve is determined by scanning a calibration phantom containing a set of tissue-equivalent materials with known ρ, which are then plotted against the measured HU values. A unique IVDT calibration curve must be created for each CT scanner and each scan mode (i.e. tube voltage, filter, etc.) [23].

2.2 Cone-Beam Computed Tomography

In fan-beam computed tomography (FBCT), approximately one-dimensional x-ray projection images are used to reconstruct a slice of the scanned object. To image a large volume, the scan acquisition and reconstruction procedure must be performed slice-by-slice. In cone-beam computed tomography (CBCT), two-dimensional x-ray projection data are used to reconstruct a full three-dimensional image, allowing for the

acquisition of volumetric data in a single rotation of source and detector. Figure 2.1 shows a simplified diagram of a CBCT system.

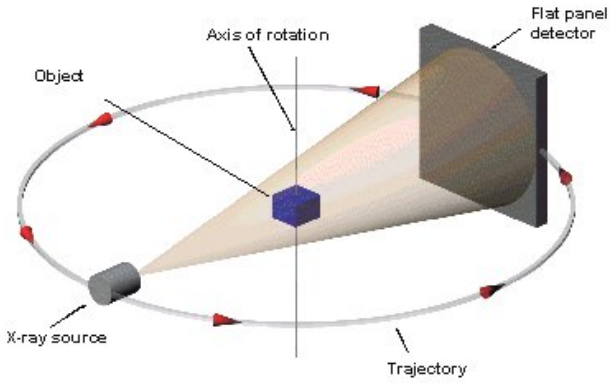

Figure 2.1: In a cone-beam CT scanner, a 2D flat-planel detector is used to acquire projection data.

2.2.1 CBCT Setup

The components and geometry of a CBCT system are very similar to that of a conventional FBCT scanner, as listed in Section 2.1.1. The main differences between FBCT and CBCT systems are in the detector technology and gantry. CBCT scanners use large flat-panel imagers to acquire projection data. The most widely used flat-panel design involves an indirect conversion of x-rays to visible light via a scintillator, such as cesium iodide (CsI). This light is then received by an amorphous silicon photodiode array and converted into an electronic signal. A schematic diagram of this type of indirect converting detector is presented in Figure 2.2 [25].

When used in image guided radiation therapy, the CBCT system is mounted on the gantry of a medical linear accelerator. This geometry allows for the patient to be imaged immediately prior to treatment, in their treatment position. This setup also allows for the isocenters of the treatment beam and the imaging beam to be coincidental, reducing uncertainty in patient positioning [3].

2.2.2 Artifacts in CBCT

A CT image artifact refers to any systematic error in the measured HU compared to the true attenuation coefficients of the object in question, and leads to a degradation

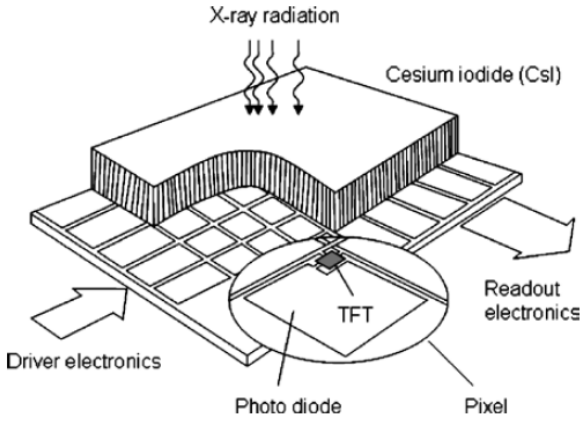

Figure 2.2: An indirect converting flat-panel detector functions by converting x-rays to visible light using CsI, and reading this light signal by a photodiode array. Pixel readout is controlled by thin-film transistors (TFTs).

of image quality. CBCT images suffer from many of the same artifacts as FBCT images, such as beam hardening, view aliasing, and patient motion [25, 26]. The beam geometry and detector technology of a CBCT scanner produces certain cone-beam related artifacts, not limited to reconstruction errors [27], overexposure [25, 26], and image lag/ghosting [28]. However, one of the most important sources of image artifacts in CBCT systems is that of x-ray scatter [29].

Conventional FBCT scanners do not suffer from scatter effects to the same degree as CBCT, due to the narrow detector array and irradiated patient volume per slice (see Figure 2.3 [30]). As the x-ray source collimation is opened, a larger volume is irradiated, increasing the production of scattered x-rays. A large flat-panel imager also increases the detection of scattered x-rays compared to a FBCT detector. In some CBCT projection images, it is possible for the scattered x-ray intensity to reach a multiple of the primary x-ray intensity [28].

Scattered x-rays manifest in CT images as scatter artifacts. Typical scatter artifacts include: lower reconstructed HU values in the center of a homogenous region (cupping); streaks and shadows across low density regions, particularly near high density objects (i.e. bone); poor low-contrast detectability; increased inaccuracy in HU determination; and an decrease of the contrast-to-noise ratio (CNR). Figure 2.4

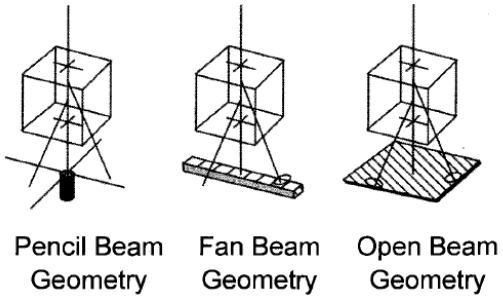

Figure 2.3: Comparison of measured x-ray scatter for a pencil, fan, and open (cone) beam geometry. As the beam geometry widens and the detector area increases, more scattered radiation is produced and detected.

demonstrates the cupping and streaking artifacts induced by x-ray scatter [28].

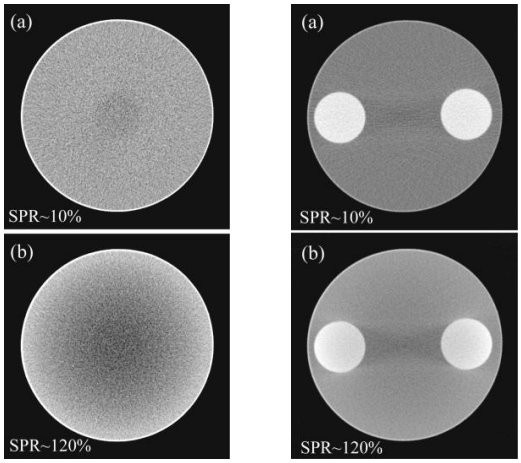

(a) Cupping (b) Streaking

Figure 2.4: Scatter-induced artifacts include "cupping" in a uniform region, and streaking between high contrast objects. The above images compare image quality under conditions of low and high scatter, indicated by scatter-to-primary ratio (SPR).

The errors in HU values derived from CBCT images are inherently unstable, as they depend greatly on the geometry of the scanned object (length and radial diameter) and scanning field of view [31, 32]. Due to this instability, a unique IVDT curve cannot be reliably determined for CBCT scanners. As such, quantitative patient dose calculations on CBCT images will be subject to errors [33].

2.3 Scatter Mitigation Techniques

Scatter reduction and mitigation in CBCT is an active area of research. For a more complete treatment of the subject, please see the review by Rührnschopf et al. [34, 35]. In general, scatter correction methods can be classified as one of three approaches: mechanical scatter rejection; measurement-based scatter correction; and model-based scatter correction.

2.3.1 Mechanical Scatter Mitigation

The first approach is to mechanically reduce scatter using hardware. An example of this type of approach is to increase the **object-detector air gap** [36]. Photons scattered by an object tend to be more divergent than the primary beam. Increasing the object to detector air gap helps to reduce the proportion of scattered to primary photons, as more scattered photons will "miss" the detector. Another mechanical scatter reduction method is the use of an **anti-scatter grid** [37]. Here, a grid made of strips of x-ray absorbing material (such as lead) is placed between the patient and the detector. The grid is aligned with the direction of the primary photon fluence (geometric rays from x-ray source to detector pixels), allowing maximum penetration of primary photons. Scattered x-rays will largely exit the patient along a direction not in line with the grid, and will be mostly absorbed. An ideal grid would allow all primary photons to pass through and absorb all scatter, however in reality there is some attenuation of primary and transmission of scattered radiation. A third common method to reduce scatter is to modulate the x-ray beam with a **compensator (bowtie filter)** [38]. Compensators are a 2D filter composed of an x-ray attenuating material (i.e. aluminum), situated at the exit window of the x-ray tube. The purpose of the compensator is to modulate the fluence of the x-ray beam such that it is more uniform once exiting the patient and reaching the detector. Pragmatically, this is done by preferentially attenuating the lateral fluence profile, while leaving the central fluence unattenuated (typically, the central fluence must penetrate through the longest path length across the patient). This lateral attenuation reduces the photon

flux through the patient, hence reducing the amount of scatter in the patient. These mechanical methods are able to suppress scatter and are employed in most CBCT systems, however they have limited efficiency.

2.3.2 Measured Scatter Subtraction

The next class of scatter-reduction approaches involves applying a scatter correction derived from a measurement-based estimation of the scatter distribution. Proposed techniques for this approach involve collimator-shadow interpolation [39] and beam stop arrays [40, 41], which measure the scatter behind shadows introduced by absorbing the x-ray beam between the source and patient. These methods assume that any measured signal in the collimator/beam stop shadow region is attributable to x-ray scatter. A 2D scatter profile can then be estimated by interpolating between projection pixel values behind the collimator/beam stop. These methods are most effective for simple, homogenous geometries which yield very smooth scatter distributions. Unfortunately, patient geometries tend to be complex and inhomogeneous, and the interpolation assumptions of these techniques leads to errors in scatter estimation. As well, beam stop array techniques require additional projection image acquisitions (with and without the beam stop array), which increases the patient imaging dose and acquisition time.

2.3.3 Model-based Scatter Subtraction

The last approach to CBCT scatter suppression is to apply a correction derived from a mathematical/physical model of scatter. These models can be based on an analytical approach to describe scatter by a convolution of a source term and a scatter propagation kernel [42]. This so-called beam-scatter-kernel approach is known to be computationally efficient, but has limited accuracy when applied to complex and heterogenous geometries [43]. An emerging topic of research in this area is the use of asymmetrically varying beam-scatter-kernels [44], whose potential has not yet been exhausted [35].

The most accurate method available to model CBCT x-ray scatter is through

a Monte Carlo (MC) simulation (see Section 3.1). In order to achieve adequate statistical uncertainty, analogue MC calculations of CBCT scatter distributions are prohibitively long [45]. In light of this, a number of accelerated MC algorithms for CBCT scatter corrections have been proposed in the literature. The method proposed by Zbijewski and Beekman [46] employs a 3D Richardson-Lucy fitting algorithm, which exploits an assumption of smooth scatter distributions in projection images. While acceptable for low scatter-to-primary ratios ($< 20\%$), this assumption begins to break down for larger objects, such as a human pelvis. Poludniowski et al. [47] attempt to reduce the number of required photon histories by using a very coarse scatter projection discretization and fixed-forced detection method. This approach also assumes the scatter distribution in each and between projections is smooth.

Rather than rely on assumptions of scatter smoothness, the method of Mainegra-Hing et al. [48] involves denoising simulated CBCT scatter projections using an adaptive filter to preserve significant features of the distribution. This is the approach taken in this study, and is explained in more detail in Section 4.1.3.

2.4 Cone-Beam Reconstruction

In order to perform an exact CT reconstruction, it is necessary for the reconstructed slice plane to intersect the source-detector trajectory at least once (the Tuy-Smith sufficiency condition) [49]. In CBCT acquired in a circular arc, exact reconstruction is then only possible for the central slice coplanar with the source-detector trajectory. Projection data acquired longitudinal from the central plane are incomplete and insufficient for an exact reconstruction method.

To address this issue, Feldkamp, Davis, and Kress [50] devised an approximate reconstruction algorithm for CBCT, known as the *FDK algorithm*. This algorithm is a generalisation of the two-dimensional fan-beam filtered backprojection, where the fan-beam is tilted out of the plane of rotation (save for the central slice)[1].

[1]There has been recent interest in developing interative techniques for cone-beam reconstruction, which better handle this missing data [51].

2.4.1 FDK In A Nutshell

For a more rigorous description of the FDK algorithm, see the original paper [50] or the treatment by Kak and Slaney [52]. In brief, the FDK algorithm breaks reconstruction into three steps. First, the measured data (tilted fan beam) are converted to a sinogram (Eq.(2.3)) and projected on to the plane of rotation, then transformed to an equivalent parallel projection. This is performed by multiplying the projection data $R_\beta(p,\zeta)$ by a weighting function:

$$R'_\beta(p,\zeta) = \frac{D_{\mathrm{SO}}}{\sqrt{D_{\mathrm{SO}}^2 + \zeta^2 + p^2}} R_\beta(p,\zeta) \tag{2.7}$$

where p and ζ are the x, y coordinates of the detector plane, and D_{SO} is the distance from the center of rotation to the source. This weighted projection $R'_\beta(p,\zeta)$ is then convolved with a filter, such as Ram-Lak, or Shepp-Logan. Finally, each filtered, weighted projection is backprojected over a three-dimensional grid, with the contribution to each voxel summed.

2.4.2 Limited View Reconstruction

In its generic derivation, the FDK algorithm (and filtered backprojection in general) assumes a complete 360° rotation of the source-detector configuration. From a geometrical argument, parallel projections which are 180° apart are mirror images of each other, thus redundant information. For fan-beam geometry, it can be shown that there is sufficient information for reconstruction using projections collected over $180 + 2\gamma_m$ degrees, where γ_m is the maximum fan angle from normal. This so-called limited view, or partial arc reconstruction is advantageous in CBCT imaging as it can reduce the radiation dose to the patient.

When using a limited view fan-beam reconstruction, some but not all projection rays will overlap (i.e. be collinear, rotated 180°). If one were to apply standard fan-beam reconstruction, these overlapping data regions would cause severe artifacts. These artifacts can be avoided by appropriately weighting the overlap regions. One such weighting method is the smooth sinogram window introduced by Parker [53].

This window, w_β, is defined as:

$$w_\beta(\gamma) = \begin{cases} \sin^2\left[\frac{45^\circ \beta}{\gamma_m - \gamma}\right], & 0 \leq \beta \leq (2\gamma_m - 2\gamma) \\ 1, & (2\gamma_m - 2\gamma) \leq \beta \leq (180^\circ - 2\gamma) \\ \sin^2\left[45^\circ \frac{180^\circ + 2\gamma_m - \beta}{\gamma + \gamma_m}\right], & (180^\circ - 2\gamma) \leq \beta \leq (180^\circ + 2\gamma). \end{cases} \tag{2.8}$$

for a given fan angle γ (angle from central ray orthogonal to detector plane), and projection angle β. Projection rays which do not overlap are weighted by unity, while overlapping rays are each weighted by a $\sin^2$ function, with the property that sum of weights is 1.

3

Materials and Methods

3.1 Monte Carlo Simulation of Photon Transport

3.1.1 Introduction to Monte Carlo Particle Transport

Accurate modelling of a computed tomography scan requires understanding the interactions of photons as they propagate through matter. While the interactions themselves are well understood, the coupled equations which describe the propagation and development of an electromagnetic shower are too complex to yield an analytical solution, unless large approximations are made. It was for finding solutions to this class of problem that the Monte Carlo (MC) method was developed by Ulam and von Neumann in the 1940s [54]. In the Monte Carlo method, the problem to be solved is first phrased as a system of probability density functions. These probability density functions are randomly sampled from (requiring the use of random numbers, hence the name "Monte Carlo"). Deterministic calculations may then be performed on the sampled events. By aggregating the results from a large number of events, an accurate solution can be reached.

For the example of particle transport, a probability distribution would describe how far a given particle would travel before interacting, and what type of interaction would occur. For an interaction where the incident particle is scattered, a probability distribution would describe the scattered particle's new energy and/or direction, and so on. Following a particle through successive interactions until it is absorbed or exits the geometry in question is known as a particle's *history*. Physical quantities of interest (i.e. dose, fluence, etc.) can be obtained by averaging over many particle

histories. As such, an MC simulation of a given quantity is essentially a counting experiment, whose statistical uncertainty depends on the number of histories simulated, N, and typically decreases with $1/\sqrt{N}$. Because of this $1/\sqrt{N}$ relation and the fact that simulating histories can be computationally intensive, reducing the statistical uncertainty to an acceptable amount can require large amounts of computational time.

In order to reduce the calculation time of MC simulation without compromising the results, MC software codes include various techniques to address this problem. One technique is *parallelization*, where the total number of desired histories is distributed over multiple CPU cores, to be run in parallel. This technique is possible since particle histories are independent from one another; the interactions during one history are assumed not to influence other histories. Parallelization is an effective way to reduce simulation time, especially if one has access to a large CPU cluster[1]. Another method of reducing simulation time is known as *variance reduction*, where physical effects are artificially weighted to increase the occurance of certain types of interactions. True variance reduction techniques reduce the number of histories (and simulation time) required to reach a desired level of statistical uncertainty, without compromising the physical accuracy of the calculation.

Variance Reduction Techniques

Some common variance reduction techniques (VRTs) for photon transport are described here. **Forced detection** is a VRT where before transporting a photon, its direction is checked to see if it intersects the scoring plane. If so, its contribution to the signal is scored in that pixel from its present position, with attenuation through the geometry taken into account. Forced detection then allows for photon signal scoring without needing to wait for the photon to reach the detector.

The **mean free path transform** is a technique that allows for more photon interactions deeper in the phantom, from where more contributions to the scatter signal

[1] There has been recent interest in exploiting the massively parallel architechture of graphics processing units (GPUs) for MC simulations.

originate. This is done by transforming the photon path length between interactions, and then weighting the interactions accordingly.

Interaction splitting refers to a technique to increase the number of scoring photons, where after an interaction, one photon is split into N photons, each with a statistical weight of $1/N$. To reduce the time wasted transporting photons aimed away from the scoring plane, a technique know as **Russian Roulette** (RR) is used to "kill" these photons, with a probability of $1-1/N$. Photons with an initial weight of 1 surviving the RR game then have a statistical weight of N. By combining interaction splitting with RR, the number of scattered photons reaching the scoring plane can be increased, while each having the same statistical weight $(1/N)$. For example, a split photon aimed away from the scoring plane and surviving RR will have a weight of $N \cdot 1/N = 1$. This photon can then interact and split again, with the second-order split photons reaching the detector having a weight of $1/N$.

To reduce the time spent transporting photons through a heterogeneous medium, **Woodcock tracing** [55], or delta transport, is a technique whereby photons have the possibility of undergoing a fictitious interaction. This fictitious interaction leaves the energy and direction of the photon unaltered, and has a cross section equal to the difference of the maximum cross section in the volume and the voxel cross section (i.e. voxels with a large cross section will have a small fictitious interaction cross section, and vice versa). This approach gives the entire geometry a homogeneous total (real + fictitious) photon cross section, allowing the photon to be transported directly to the interaction site, eliminating the need for tedious ray tracing.

3.1.2 Photon Transport with EGSnrc

The EGSnrc code [56] was developed at the National Research Council of Canada (NRC) in Ottawa, and was adapted from the EGS (Electron-Gamma-Shower) code [57] originally written for high energy physics simulations at the Stanford Linear Accelerator (SLAC) in Stanford, California. EGSnrc is a general MC particle transport code with enhancements for use in medical physics research with electron or photon beams. In the EGSnrc code, photons may interact with the surrounding media by four pro-

cesses: photoelectric absorption, incoherent (Compton) scattering with atomic electrons, coherent (Rayleigh) scattering with molecules/atoms, and pair/triplet production. In photoelectric absorption, or the photoelectric effect, a photon is completely absorbed by an atom and an electron is emitted with a kinetic energy equal to the incident photon energy minus the electron binding energy. Compton scattering describes the scattering of a photon off of a loosely-bound orbital electron, yielding a scattered photon and recoil electron. After Compton scattering, the energy of the incident photon is shared between the kinetic energy of the recoil electron and the scattered photon. In Rayleigh scattering, a photon is scattered off of an entire molecule (or atom). Rayleigh scattering is an elastic process, where the scattered photon has the same energy but different direction as the incident photon. Pair production occurs when a high energy photon ($h\nu$ >1.02 MeV) interacts with the electromagnetic field of an atomic nucleus, producing an electron-positron pair. An analogous process can occur ($h\nu > 2.04$ MeV) in the electromagnetic field of an atomic electron and is known as triplet production, as the atomic electron recoils and becomes a third emitted particle. At diagnostic x-ray energies ($h\nu < 200$ keV) in tissue, Compton scattering is the dominant photon interaction, and pair and triplet production can be ignored.

The cross-sections for the above interactions are dependent on material and photon energy. To calculate cross-sections, EGSnrc reads in material data provided by a stand-alone program called PEGS4 [58]. PEGS4 interpolates material cross-section data given certain parameters, such as elemental composition, density, and photon and electron energy cutoffs. EGSnrc allows the user to influence the calculation time and simulation accuracy by setting an electron and photon cutoff energy, ECUT and PCUT. If the energy of a given electron/photon after an interaction falls below ECUT/PCUT, then the particle's history is terminated and its energy is deposited locally. By setting ECUT and PCUT to be very low, detailed simulations are possible at the expense of simulation time. If ECUT is set to be greater than the maximum photon energy, secondary electrons will not be transported, and their energy will be

deposited on the spot.

3.2 Varian OBI CBCT Scanner

All CBCT images in this study were acquired using a Varian Medical Systems (Palo Alto, CA) On-Board Imager® (OBI) system. The OBI is a kV CBCT imaging system attached to a linear accelerator gantry, offset by 90 degrees with the MV treatment beam. Images are acquired using an 39.7 × 29.8 cm amorphous silicon flat-panel detector. Mounted on the flat-panel detector is a 10:1 anti-scatter grid.

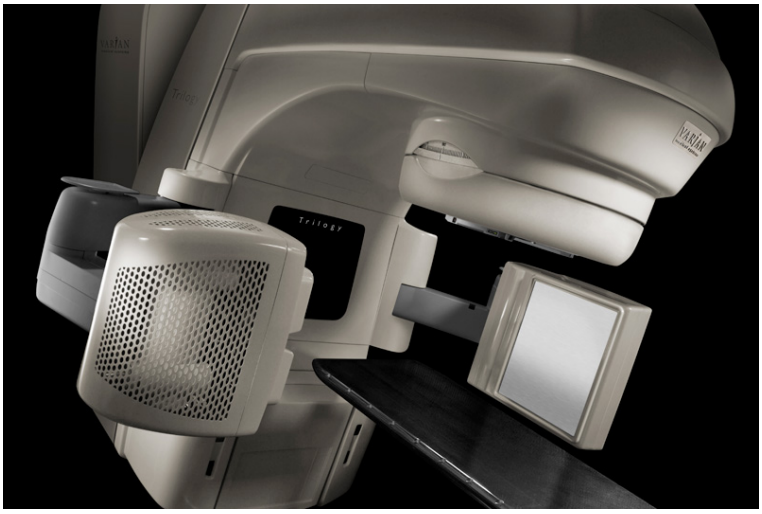

Figure 3.1: The Varian On-Board Imager kV imaging system (OBI) consists of a kV x-ray source and flat-panel imager mounted to a linac gantry. Courtesy of Varian Medical Systems (Palo Alto, CA).

The standard-dose head imaging protocol was used exclusively in this work, which consists of acquiring 360 projections[1] over a 200 degree arc. X-ray tube settings for this protocol are a peak tube voltage of 100 kVp, a tube current of 20 mA, and an exposure time of 20 ms for each projection. The geometry of this protocol uses the so-called full fan acquisition mode (see Figure 3.2). The reconstructed field of view in this mode is a cylinder of 24 cm diameter (axial), and 18 cm height (longitudinal).

[1]It was found that the actual number of acquired projections varied from scan to scan, ranging from 358 to 361 projections.

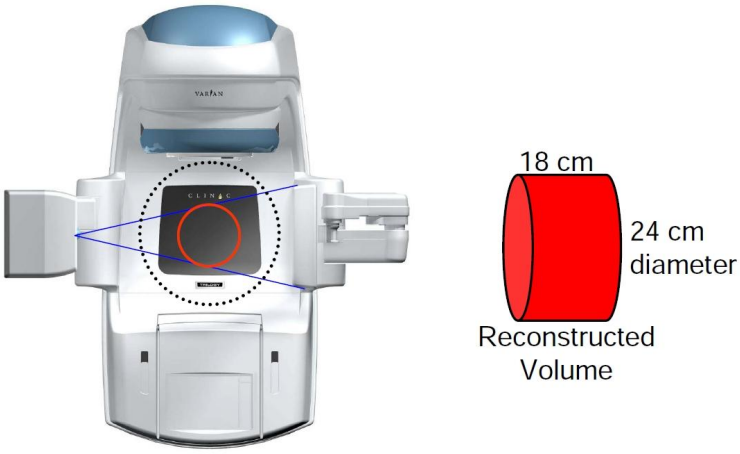

Figure 3.2: Representation of the reconstructed field of view for the Varian OBI system during full fan acquisition. Courtesy of Varian Medical Systems (Palo Alto, CA).

In the MC simulation of the CBCT system, the modulation effects of the bowtie filtered were not modelled. As such, all CBCT scans used in conjunction with the scatter correction had the bowtie filter removed from the x-ray beam. Inclusion of the filter in the MC simulation is left for future investigation. The bowtie filter was, however, installed for CBCT scans where it was desired to obtain the reconstructed image provided by the Varian OBI reconstruction software, which assumes the filter to be in place.

3.2.1 OBI CBCT Calibration

The OBI system has a number of calibrations and corrections applied to improve imaging performance.

A **geometry calibration** is applied to correct for machine instability (i.e. motion of kV source and detector arms) during scans. This calibration is used to estimate the kV isocenter, and is performed during the installation of the OBI system. The geometric accuracy of the system is checked daily to weekly.

An **imaging system calibration** determines the linearity of each pixel and sets the threshold for dual gain readout[1]. A pixel defect map is also created during this

[1]Dual gain readout is a mode where pixels are read out twice, once at low and high sensitivities. By selecting unsaturated pixels, high dynamic range can be obtained.

calibration. This calibration is performed during installation.

An $\mathbf{I_0}$ calibration is an air scan, which measures the unattenuated flux per pixel. This calibration also helps to reduce ring artifacts. It is recommended that this calibration be performed quarterly, or when necessary.

A **beam hardening correction** corrects for the increase in energy of the kV beam as it passes through the patient. Varian provides default beam hardening correction values.

A **normalisation scan** is performed to account for radiation scatter and beam hardening. It is essentially an I_0 calibration, only through a normalisation phantom of known geometry and composition. It is recommended that this calibration be performed quarterly to maintain image quality.

The **Hounsfield Unit calibration** maps correct HU numbers to reconstructed voxel values. This calibration is applied only after the normalisation, geometry, and pixel defect corrections have been carried out. The HU calibration is performed during installation.

3.2.2 Blank Scan

A blank scan, air scan, or "flood field" is a CT transmission scan performed without an object in the field of view. A blank scan is required to properly calculate attenuation coefficients during CT reconstruction (see Eq.(2.1)). Blank scans are typically performed during the commissioning of a CT scanner, or as part of a quality assurance program. In this work, our own blank scan was performed using the standard-dose head protocol, with the linac couch retracted out of the field of view.

3.2.3 Phantom Scan

To acquire a phantom scan, a phantom was first set up on the linac couch and positioned in center of the OBI field of view using room-mounted positioning lasers. Care was taken to ensure that metallic objects, such as clips and rails attached to the couch, were not in the radiation field as they could act as an x-ray scatter source.

In this work, phantom scans were performed following a blank scan. This order is

recommended for the combined purpose of warming up the x-ray tube, and saturating the amount of charge trapping in the flat-panel detector. Near saturation, the trapped charge levels stabilise, reducing charge trapping image artifacts [59].

3.3 CT Phantoms

3.3.1 Solid Water

Solid Water® (Gammex, Middleton, WI) is a plastic material which has a similar density ($\rho_{\text{sw}} = 1.04$ g/cm^3) and ionizing radiation absorption characteristics as water. Its ease in handling and positioning, as well as its ability to be machined into custom dimensions, makes it a convenient substitution to water tank phantoms. Slabs of Solid Water were used as an attenuating phantom to test the FDK reconstruction program, as well as the initial implementation of the scatter correction algorithm.

3.3.2 ACR CT Accreditation Phantom

The ACR CT Accredication Phantom (Gammex, Middleton, WI) is a solid cylindrical phantom designed to be part of the American College of Radiology CT accreditation program (see Figure 3.3). The phantom is meant to be used for CT scanner quality assurance assessment and testing. It is composed primarily out of Solid Water and contains modules designed to allow the measurement of CT number accuracy and uniformity, low and high contrast resolution, slice thickness, alignment, and positioning. To test CT number accuracy, one module contains four imbedded test objects; bone (tissue equivalent material), acrylic, low density polyethylene, and air. The phantom has a length of 16 cm and diameter of 20 cm, which easily fits in to the field of view of the Varian OBI CBCT.

3.3.3 RANDO Head Phantom

The RANDO® head phantom (The Phantom Laboratory, Salem, NY) is an anthropomorphic head phantom, consisting of a real human skeleton cast inside a soft tissue-simulating material. This phantom allows for experimental measurements in a real-

Figure 3.3: The ACR CT Accreditation Phantom (Gammex, Middleton, WI) with support base.

istic anatomical geometry. The tissue-simulating material has a mass density and effective atomic number similar to that of fat-distributed muscle tissue, giving it radiotherapy photon attenuation properties similar to real human tissue. An image of a RANDO head phantom similar to the one used in this study is shown in Figure 3.4.

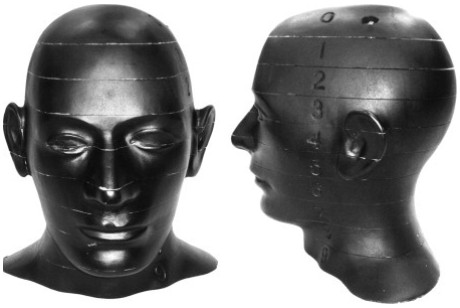

Figure 3.4: The RANDO® head phantom (The Phantom Laboratory, Salem, NY) is constructed with a human skeleton cast inside a soft tissue equivalent material.

4

CBCT Scatter Correction Algorithm

4.1 Scatter Correction Algorithm

A scatter correction was applied, adapted from the algorithm proposed by Mainegra-Hing et al [60]. The steps of the algorithm are as follows:

1. Perform 3D reconstruction of the raw projection data, using the FDK algorithm.
2. Convert reconstructed voxel attenuation coefficients (μ) to material densities.
3. Import density matrix to EGSnrc simulation (`egs_cbct`), and compute primary and scatter projections.
4. Apply scatter correction to projection pixel data.
5. Perform 3D reconstruction of the corrected projection data.

After reconstruction, the scatter corrected image was analysed for improvements in image quality. A flowchart of the correction algorithm is shown in Figure 4.1.

It is worth noting that in its original form, the proposed scatter correction algorithm was intended to be applied iteratively, with the corrected voxels of Step 5 becoming input to Step 2. The iteration would then be stopped when a convergence of the reconstructed image was reached. In the original paper by Mainegra-Hing et al, the termination criteria for convergence was determined by manual inspection. In the work presented, it was found that the iterative algorithm was unable to reach a convergence. The algorithm was instead applied non-iteratively, as described above.

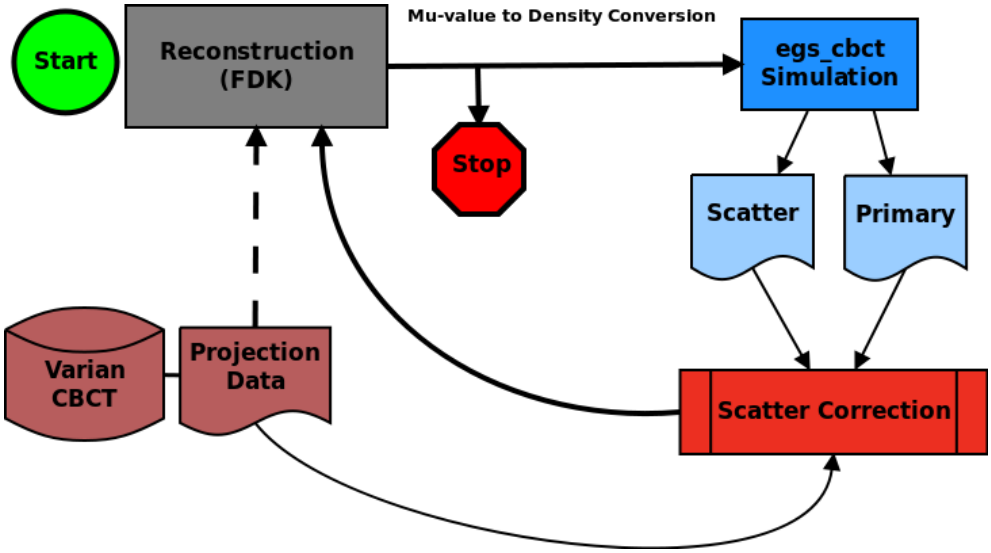

Figure 4.1: Flowchart of scatter correction algorithm.

The failure of the iterative approach is most likely due to the deviation from ideal conditions assumed in Mainegra-Hing's study, such as the presence of real image noise, and the effects of the anti-scatter grid.

4.1.1 Image Reconstruction

After acquiring a CBCT scan, the raw projection data was extracted from the Varian OBI reconstructor computer. Due to limited hard disk space and the large file sizes (∼500 Mb to 1 Gb per scan), by default projection data is only stored on the reconstructor computer for 48 hours, after which time it is automatically deleted. Varian OBI projection data is stored in a proprietary HNx format, where each projection image file consisted of a file header, followed by compressed pixel data. A program supplied by Varian was used to uncompress the pixel data to a more readable format, where they were stored as 16-bit unsigned integers. The uncompressed projection image files were then stripped of their headers, leaving only pixel data. The resolution of the acquired projection images was 1024 by 768 pixels, with pixel dimensions of 0.388 mm × 0.388 mm.

To decrease noise in the reconstructed image, the projection images were subjected to smoothing. Figure 4.2 highlights the effect projection smoothing has on reducing

noise in reconstructed data. Air scan projections were smoothed with a Gaussian filter ($\sigma = 5$ pixels). Smoothing of phantom scan projections was investigated using either a Gaussian or median filter. While both filters achieved similar results in noise reduction, the median filter was found to better preserve sharp edges after reconstruction. In the results presented, phantom scan projections were smoothed with a median filter (radius = 4 pixels).

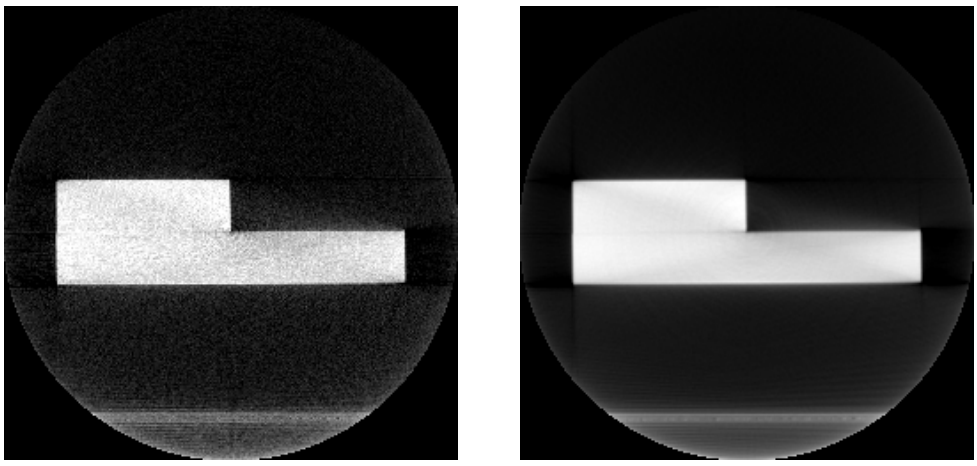

(a) No smoothing (b) Smoothing

Figure 4.2: Reconstructed CBCT slices of the slab phantom using (a) unsmoothed and (b) smoothed projection data.

Image reconstruction was performed by first calculating the sinogram (Eq.(2.3)), and using an implementation of the filtered back projection algorithm of Feldkamp, Davis, and Kress (FDK) [50], following the prescription of Kak and Slaney [52]. Partial arc reconstruction was handled by weighting overlapping projections with a smooth sinogram window (see Section 2.4.2). To prevent segmentation faults due to lack of physical memory, a memory-efficient convolution function was written (see Appendix A).

A Shepp-Logan filter was used as the convolution filter to minimise blurring and help reduce high frequency noise. The convolution of the Shepp-Logan filter with projection data was parallelised using the OpenMP application programming interface [61]. The reconstructed volume consisted of 64, 2.7 mm thick longitudinal slices, with 384 by 384 voxels per slice (0.67 mm $\times$ 0.67 mm).

4.1.2 CT-to-Density Conversion

To accurately transport particles through a CT-acquired geometry using a Monte Carlo simulation, each voxel of the CT image must be associated to a material type and mass density (ρ). After reconstruction, CT voxels represent the average photon attenuation coefficient (μ) for that volume. This means that the μ of each voxel must be converted into a ρ and material. At kilovoltage energies, there is no direct relationship between μ and ρ for human tissues, thus accurate conversion from attenuation coefficient to mass density and material is not straightforward [22].

In this study, material type was assigned according to a μ window. For each CBCT-scanned object, a ramp file was created containing relevant material types, their nominal attenuation coefficients, and densities. Material attenuation coefficients were calculated using the EGSnrc user code `g`, using the same material definitions from the CBCT simulation (Section 4.1.3). In the ramp file, materials were arranged in order of increasing μ. A simplistic method was used to determine a material's μ range. The lower and upper μ limits were determined by the average μ of successive materials. For example, given a ramp file with three materials in order of ascending μ (Material A, B, and C), the upper μ limit for Material A (and lower limit for Material B) would be the average μ for Material A and B. Likewise, the upper μ limit for Material B (lower limit for Material C) would be the average μ for Material B and C. Effectively, this method sets the μ range limits to be the μ midpoints between successive materials. Voxel material assignment was determined by sorting μ values into the appropriate material μ window. In a simple example, consider two materials: Material A, with a μ window from 0.1 to 0.25 cm^{-1}; and Material B, with a μ window from 0.25 to 0.5 cm^{-1}. For a given voxel with $\mu = 0.21$ cm^{-1}, it would be assigned as Material A.

Once voxels had been assigned a material type, mass density was then determined. Voxel mass density was calculated by a fractional method, where for a voxel with μ_i assigned as a material with μ_{mat}, density was found as

$$\rho_i = \frac{\mu_i}{\mu_{\text{mat}}} \rho_{\text{mat}}. \tag{4.1}$$

In this way, the ratio of μ_i to μ_{mat} is recovered in the EGSnrc simulation by dividing ρ_i by ρ_{mat}.

4.1.3 MC Simulation of CBCT

The CBCT simulation was performed using the `egs_cbct` user code, developed by Ernesto Mainegra-Hing. Written in C++, `egs_cbct` uses the EGSnrc C++ class library [62]. The simulation consists of a photon source and voxelized phantom geometry, with a scoring plane in place of the flat-panel detector. At the detector plane, air-kerma[1] is scored by track-length estimation, where all photons crossing the plane contribute to the kerma. This method has been shown to be 20 times more efficient than the typical calculation of kerma by measuring the energy deposited by electrons on the spot [63]. The user code is able to identify the air-kerma contribution from primary and scattered photons. To increase the efficiency of the simulation, photons are simulated down to 1 keV (PCUT = 1 keV), and electron transport is turned off. Photons are allowed to interact via photoelectric effect, coherent (Rayleigh) scattering, and incoherent (Compton) scattering. Compton interactions are modeled according to the Klein-Nishina equation, and material photon cross-sections were calculated from the XCOM database [64].

To further improve the efficiency of CBCT scatter estimation, `egs_cbct` makes use of a number of variance reduction techniques (VRTs). For a complete description of all the implemented VRTs, please see [48]. Every time a photon is directed towards the scoring plane, its contribution is scored (including the effects of attenuation), in a technique known as *forced detection*. To enhance the number of interactions occuring deep in the phantom where most of the scatter signal originates, a photon path length transformation scheme was devised (a.k.a *mean free path transform*). A combination of *interaction splitting* and *Russian Roulette* helps to increase the number of scoring particles (i.e. those directed towards the scoring plane), while reducing the variance

[1] **Air-kerma** is defined as the mean energy transferred from photons to charged particles per unit mass, in air. Below megavoltage energies in low-Z materials, air-kerma is essentially equivalent to absorbed dose.

of the scored air-kerma. Photons travelling away from the detector which survive Russian Roulette are transported using *Woodcock tracing*, which further minimises the time spent transporting photons which are unlikely to contribute to the CBCT signal.

In an effort to further decrease simulation time, the scatter air-kerma distribution was subjected to denoising using a 2D locally-adaptive Savitzky-Goley filter, developed by Kawrakow [65]. Originally developed to smooth Monte Carlo calculated dose distributions, this filter uses an adaptive smoothing window size determined by significance tests to reduce the probability of systematic bias. Mainegra-Hing reported that due to the fact that scatter distributions are generally well behaved without sharp discontinuities, this choice of denoising algorithm performs very well [60].

In the estimation of CBCT projection data, the parameters of the `egs_cbct` simulation were made to match the configuration of a Varian OBI CBCT system as closely as possible. The photon beam was modeled as a point source, using a 100 kVp tungsten target with filtration x-ray spectrum. This generic diagnostic x-ray spectrum was assumed to match the main beam characteristics of the Varian x-ray tube, and only small variations in low-energy photon fluence due to differences in filtration are expected. For completeness, a full simulation of the x-ray tube photon fluence distribution and spectrum without the presence of the bowtie filter [66] would be valuable, however such a study was out of the scope of this work.

The point source was located 100 cm from the simulation isocenter, and the detector scoring plane was centered at 148.99 cm from the source along a line connecting the source to isocenter. The center of the voxelised phantom geometry was set coincident with the CBCT isocenter, such that the source-detector system could be rotated around the phantom for CBCT acquisition. The dimensions of the scoring plane (39.7 cm by 29.8 cm) were made to match the dimensions of the CBCT flat-panel detector. In this work, the flat-panel detector was assumed to be 100% efficient and independent of energy. In reality, the detector has an energy response function and limited

efficiency[1]. As well, photon and electron interactions inside the detector structures (i.e. amorphous silicon layer) which give rise to glare artifacts were ignored. It can be assumed that these are second-order effects when compared to the overall scatter correction. For future study, it is recommended that a complete simulation of the detector panel be investigated.

For each simulated scan, the number of simulated projections was identical to the measured scan (approximately 360 projections over an arc of 200 degrees). In this study, an efficient rectangular beam with source biasing was used to irradiate the whole detector area, defined in the EGS particle source library. For this type of beam, the user defines a rectangular grid which projects on to the dimensions of the detector scoring plane, and the source chooses a random position inside each pixel. For each simulated projection image, 52428800 particle histories were run. This number of histories gave an average statistical uncertainty of 1.3% for primary scans, 6.4% (pre-smoothing), and 0.4% (post-smoothing) for scatter scans. Running on a single core of a 2.66 GHz Intel Xeon processor, simulation of one projection angle took 10 minutes.

To increase simulation efficiency at the cost of spatial resolution, the detector scoring plane was segmented into 256×192 pixels instead of the 1024×768 pixels found in the real CBCT projection images. Once the CBCT simulation was complete, the projection images were upsampled to 1024×768 pixels, using bicubic interpolation. In the first approach, the real projection images were downsampled to 256×192, however this was found to introduce aliasing artifacts in the FDK reconstruction.

4.1.4 Scatter Correction

The scatter correction used in this work was adapted from the approach used by Mainegra-Hing et al [60]. Its derivation is as follows:

From the Beer-Lambert law of exponential attenuation

$$I_{i,\text{att}} = I_{i,\text{air}} e^{-\int \mu(\ell) \mathrm{d}\ell}, \tag{4.2}$$

where $I_{i,\text{air}}$ and $I_{i,\text{att}}$ are the intensity from primary photons for an air (unattenuated)

[1]Here, I define detector efficiency as the ratio of measured air-kerma to true air-kerma.

or phantom (attenuated) scan, respectively, and $\mu(\ell)$ is the x-ray attenuation coefficient at position ℓ along a line connecting the x-ray source to detector pixel i. We can then define the scatter-free quantity a_i:

$$a_i = \ln\left(\frac{I_{i,\text{air}}}{I_{i,\text{att}}}\right) = \int \mu(\ell)\mathrm{d}\ell. \tag{4.3}$$

In this form, a_i represents the attenuation of primary photons along a path from source to detector.

In reality, a detector pixel will measure intensity from both primary and scattered photons, or total intensity $I_{i,\text{tot}}$;

$$I_{i,\text{tot}} = I_{i,\text{att}} + I_{i,\text{scat}}. \tag{4.4}$$

If one assumes that the major differences between the measured and simulated pixel signal intensity are due to differences in simulation attenuation properties, it follows that

$$\frac{I_{i,\text{att}}}{\tilde{I}_{i,\text{att}}} \approx \frac{I_{i,\text{tot}}}{\tilde{I}_{i,\text{tot}}} \tag{4.5}$$

where symbols with a tilde denote Monte Carlo derived quantities. Substituting (4.5) into (4.3) gives

$$a_i = \ln\left(\frac{I_{i,\text{air}}}{I_{i,\text{tot}}}\right) + \ln\left(\frac{\tilde{I}_{i,\text{tot}}}{\tilde{I}_{i,\text{att}}}\right). \tag{4.6}$$

Define the measured quantity r_i as:

$$r_i = \ln\left(\frac{I_{i,\text{air}}}{I_{i,\text{tot}}}\right), \tag{4.7}$$

and recalling (4.4), we can then rewrite (4.6) as

$$a_i = r_i - \ln\left(\frac{\tilde{I}_{i,\text{att}}}{\tilde{I}_{i,\text{att}} + \tilde{I}_{i,\text{scat}}}\right). \tag{4.8}$$

To compensate for errors introduced by the assumption of (4.5), a relaxation term of $\alpha(r_i - \tilde{r}_i)$ is added, with α a free parameter. A selection of $\alpha = 0$ would then ignore the attenuation differences between the simulation and measured scan. To account for

the presence of an anti-scatter grid, the simulated scatter intensity is modulated by a tunable grid parameter, β. In this simple form, a setting of $\beta = 1$ would represent the absence of an anti-scatter grid, and $\beta = 0$ an ideal grid which removes all scattered x-rays.

The scatter-free quantity in its final form is then given by

$$a_i = (1 + \alpha)r_i - \alpha\tilde{r}_i - \ln\left(\frac{\tilde{I}_{i,\text{att}}}{\tilde{I}_{i,\text{att}} + \beta\tilde{I}_{i,\text{scat}}}\right). \tag{4.9}$$

In this study, the scatter correction was performed by calculating the scatter-free projection pixel value a_i from Eq.(4.9), for all pixels in each projection image.

5

Results

5.1 Slab Phantom

5.1.1 FDK Reconstruction

As a first test of the process to extract Varian OBI projection data and perform a standalone FDK reconstruction, a simple phantom consisting of two Solid Water® (Gammex, Middleton, WI) slabs was scanned. The two slabs ($20\times20\times3$ cm^3 and $10\times10\times3$ cm^3) were placed flat on the treatment couch, with the smaller slab placed on top of the larger slab and aligned to be coincident at a superior corner. The phantom was positioned such that the CBCT isocenter was situated directly between the two slabs, on the surface center of the larger slab. To reduce backscatter effects originating from the treatment couch, the phantom was elevated off of the couch by a 7 cm thick slab of low density polystyrene foam.

The slab phantom projection data were successfully retrieved from the Varian OBI reconstructor computer system (see Figure 5.2a for a sample projection), and reconstructed using an implementation of the FDK algorithm, as described in Section 4.1.1. It was noticed that the reconstructed image contained streaking and striping artifacts along the edges of the phantom and treatment couch (see Figure 5.2b). It was determined that these artifacts were caused by view aliasing at sharp, flat edges. In light of this information, a cylindrical phantom without sharp edges was used in the next step of the study (ACR CT accreditation phantom).

It was noticed during the acquisition and analysis of the blank scan that the projection images did not all have the same average intensity. For each progressive

projection the average pixel value tended to increase, quite rapidly for the first ∼30 projections, then more gradually for the remainder of the scan. This trend is shown in Figure 5.1, and is most likely due to charge trapping from successive projection irradiations in the flat-panel detector. While charge trapping cannot be eliminated completely, it is recommended that the detector be saturated prior to performing a scan so that the amount of charge trapping is roughly constant in each projection image. From Figure 5.1, in the linear region (Projection #30 an onward) this effect increases the average projection intensity by 3%. In this work, no explicit correction was made to account for charge trapping. It was assumed that this effect would be cancelled out by taking the ratio of phantom and blank projections (Eq.(2.3)) prior to reconstruction.

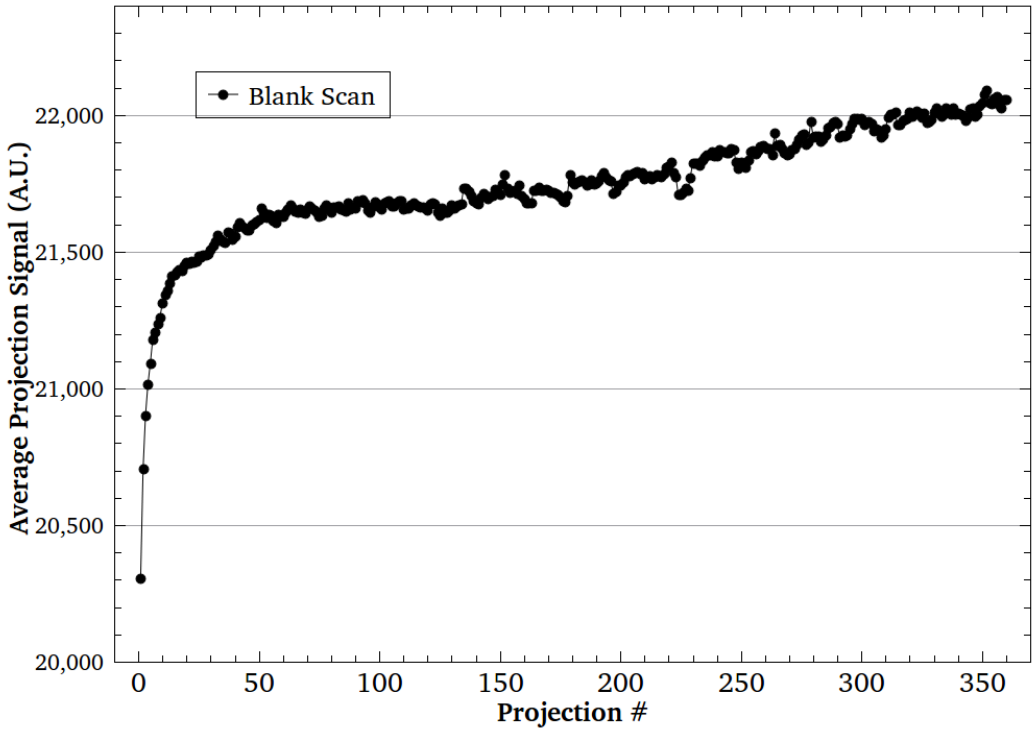

Figure 5.1: Average pixel intensity per blank projection image, plotted as a function of sequential projection number. The average projection intensity increases over time due to charge trapping in the flat-panel detector.

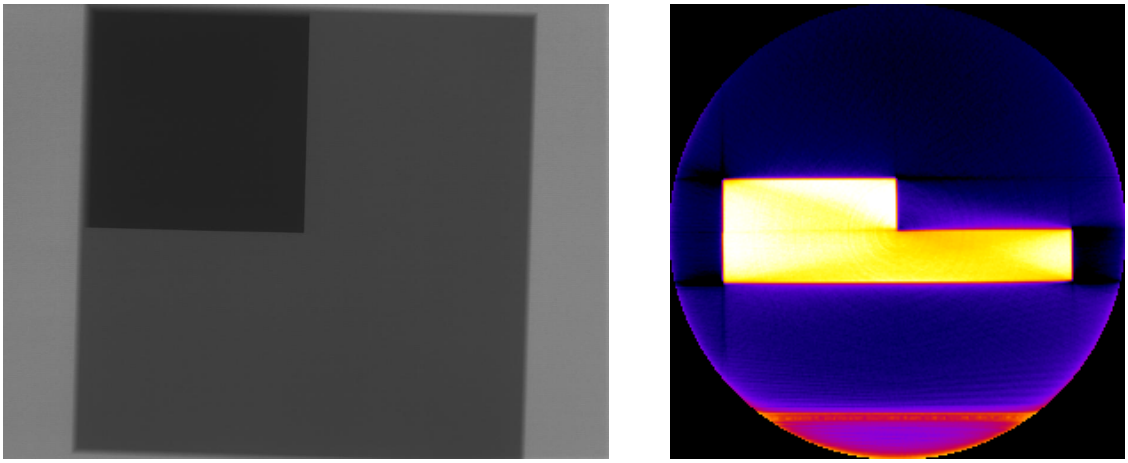

(a) Projection image (b) Reconstructed slice

Figure 5.2: (a) An example of a raw projection image of the Solid Water slab phantom, acquired from the Varian OBI system. (b) FDK reconstructed slice from raw data. Note streaks due to view aliasing along sharp edges of the phantom and treatment couch.

5.1.2 Scatter Correction: Proof of Concept

Despite the view aliasing artifacts, the scatter correction algorithm described in Chapter 4 was applied to the slab phantom data as a proof of concept. The reconstructed voxels were assigned to a material type according to the μ ranges listed in Table 5.1, based on the known materials present in the scan (air, Solid Water, etc.). Once assigned to a material, the voxel attenuation coefficients were converted to a mass density following Eq.(4.1). In this application of the scatter correction formula (Eq.(4.9)), parameter values of $\alpha = 0.5$ and $\beta = 1$ were chosen.

The results of the scatter correction on the reconstructed image can be seen in Figure 5.3. An attenuation profile across one slice of the reconstructed phantom (Figure 5.3a) was compared between raw (uncorrected) and scatter corrected projection data for two iterations of the scatter correction algorithm (Figure 5.3b). In this profile, the scatter correction appears to be reducing the streaking artifact across the air step between the two Solid Water slabs, resulting in a sharper edge at the air/phantom boundary. The correction also has the effect of increasing the reconstructed attenuation coefficients in the Solid Water (main source of scattering), while largely ignoring the air, polystyrene foam, and treatment couch attenuation coeffi-

Table 5.1: Solid Water slab phantom ramp file used for conversion of reconstructed attenuation coefficients to materials and mass densities. The material ICRU Carbon was used as an estimate of carbon fiber.

Material	μ **Range** [$\mathbf{cm^{-1}}$]	ρ [$\mathbf{g/cm^3}$]
Vacuum	[-1.0 : 1.0E-7]	0.0
Air	[1.0E-7 : 0.005]	1.205E-2
Polystyrene Foam	[0.005 : 0.11]	5.0E-2
Solid Water	[0.11 : 0.265]	1.03
ICRU Carbon	[0.265 : 1.5]	1.7

cients. However, it is difficult to quantify the improvement in image quality due to the scatter correction using this simple phantom. Encouraged by these results, the study was continued on a more complex phantom.

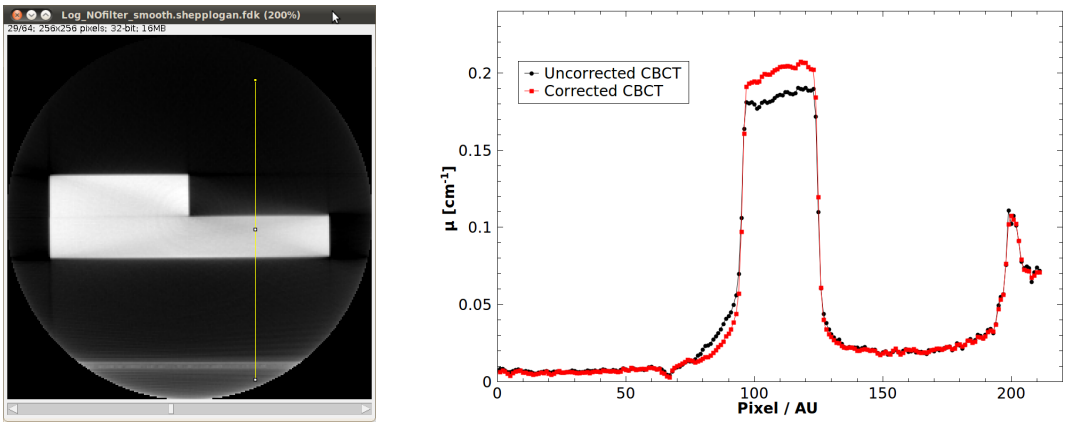

(a) Slab phantom slice

(b) Profile across slab phantom

Figure 5.3: Results of scatter correction shown for a profile across the Solid Water slab phantom.

5.2 ACR Accreditation Phantom

As the next step in the study, an ACR CT accreditation phantom (Gammex, Middleton, WI) was scanned on the Varian OBI system. In addition to the cone-beam CT scan, the ACR phantom was also scanned on a conventional fan-beam CT scanner (Philips Brilliance Big-Bore CT (Philips Healthcare, Andover, MA)) used for patient

treatment planning in the Montreal General Hospital. The planning CT images were acquired at 120 kVp, 500 mAs, 3 mm slice spacing, and an FOV of 30 cm. This allowed for the scatter corrected CBCT images to be compared with "clinical ground truth" fan-beam CT data.

The raw CBCT projection data was acquired and reconstructed, then reconstructed CBCT voxels were assigned to a material and converted to mass density according to Table 5.2, taking into account the various materials present in the ACR phantom. Next, primary and scatter projection images were generated with `egs_cbct` for each projection angle. Figure 5.4 shows an example of the simulated projection data for primary (a) and scattered (b) photons. The excellent denoising effect of the scatter smoothing procedure is demonstrated in (c).

Table 5.2: ACR phantom ramp file used for conversion of reconstructed attenuation coefficients to materials and mass densities.

Material	μ **Range** [$\mathbf{cm^{-1}}$]	ρ [$\mathbf{g/cm^3}$]
Vacuum	[-1.0 : 1.0E-7]	0.0
Air	[1.0E-7 : 0.005]	1.205E-2
Polystyrene Foam	[0.005 : 0.0967]	5.0E-2
Polyethylene	[0.0967 : 0.2044]	0.93
Solid Water	[0.2044 : 0.23]	1.03
PMMA	[0.23 : 0.448]	1.19
ICRU Bone	[0.448 : 0.817]	1.56
Aluminum	[0.817 : 7.24]	2.702
Steel	[7.24 : 50]	8.06

For proper comparison with the fan-beam CT images, the CBCT reconstructed voxel attenuation coefficients were converted to appropriate CT numbers, or Hounsfield units (HU). For the planning CT scanner used, the HU range spanned from 24 to 4119, with water set to 1024. This HU convention was calculated by modifying Eq.(2.5) to

$$HU = 1000 \times \left(\frac{\mu_i - \mu_{\text{water}}}{\mu_{\text{water}}} \right) + 1024, \tag{5.1}$$

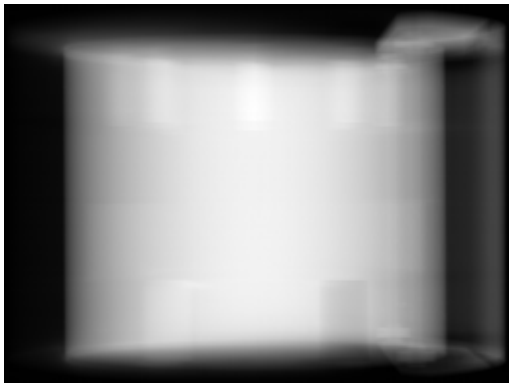

(a) Primary projection

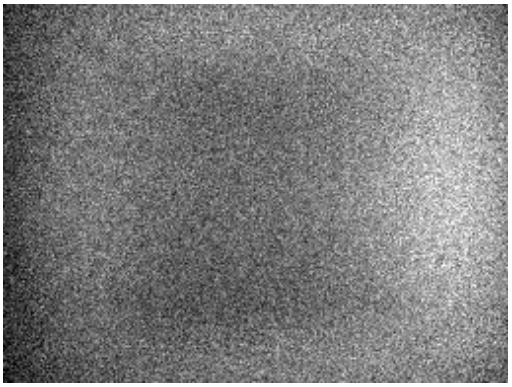

(b) Scatter projection

(c) Scatter projection with smoothing

Figure 5.4: Primary (a) and scatter (b) component projections of the ACR phantom simulated by `egs_cbct`. The effect of the scatter smoothing procedure is shown in (c).

for each given voxel i. To convert CBCT voxels to HU using Eq.(5.1), a value of $\mu_{\text{water}} = 0.219$ cm^{-1} was used. This μ value was calculated using the EGSnrc user code, `g`, with the same 100 kVp spectrum employed in the `egs_cbct` simulation.

5.2.1 HU Uniformity

One module of the ACR phantom consists of a single uniform disc of Solid Water, for use in assessing HU uniformity of CT images. As a measure of uniformity, a profile was taken across the center of the reconstructed phantom in this module. As can be seen in Figure 5.5, the raw CBCT data exhibits a large cupping artifact in this uniform region, where the voxels in the center of the phantom are reconstructed with lower μ values. After applying the scatter correction, the cupping artifact is greatly

mitigated. This would suggest that the observed cupping artifact was mainly caused by scatter into the center of the phantom for each projection, leading to a higher signal in this region and thus a lower reconstructed μ. For comparison, a profile across the fan-beam CT data is also shown, rigidly registered with the CBCT data. While the scatter corrected CBCT profile agrees well with the FBCT data, it appears that there is a small HU offset in the reconstructed μ of Solid Water between them. There is also a difference in the reconstructed μ of air, shown by the profile in the peripheral regions outside of the phantom. In both uncorrected and scatter corrected CBCT images, the reconstructed μ of air voxels are larger than the values from the FBCT scan.

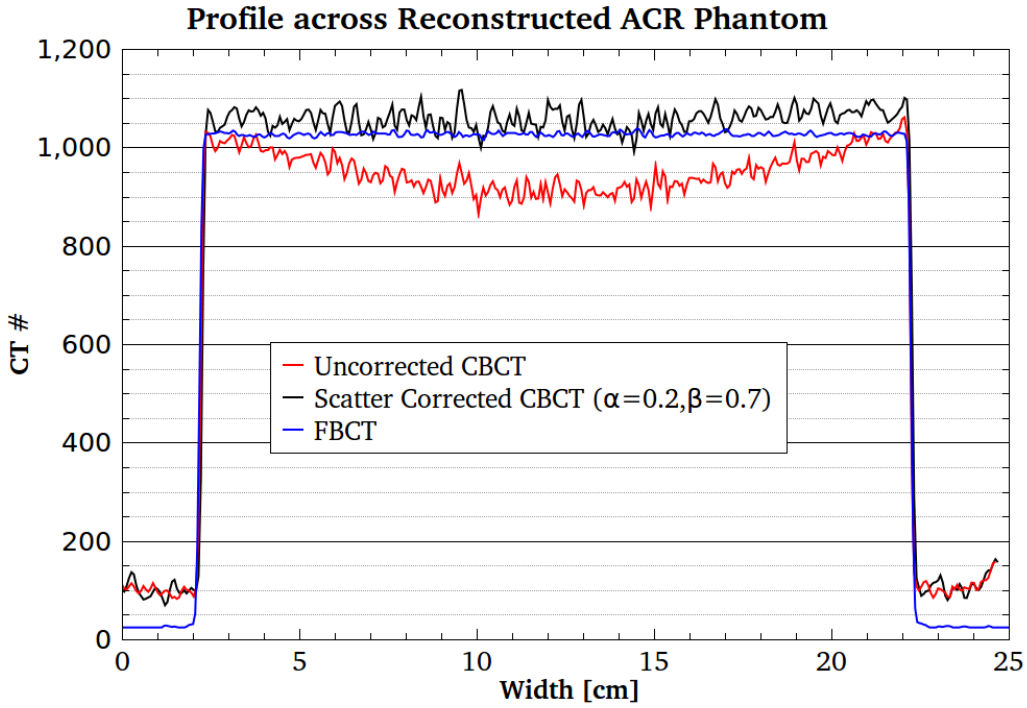

Figure 5.5: Profile across the center of a uniform region in the reconstructed ACR accrediation phantom for raw and scatter corrected CBCT data. Fan-beam CT profile is included for comparison.

As another test of the performance of the scatter correction, the HU uniformity profile from the corrected CBCT data was compared against that from the reconstructed CBCT image provided by the Varian OBI software. While this software

includes a number of corrections (see Section 3.2.1), it does not explicitly account for scatter effects. The results of a profile comparison are shown in Figure 5.6. It can be seen that the OBI reconstructed profile in the Solid Water region has an average μ which agrees well with the FBCT data, however the profile is very noisy (up to $\pm$250 HU difference from the mean). On the lateral edges of the phantom, the OBI profile has a dip on one side and a bump on the other side (at positions of 5 and 20 cm in Figure 5.6, respectively). These perturbations from uniformity are due to a crescent artifact caused by the presence of the bowtie filter. It appears that a correction is applied to the OBI voxels in air, which are uniformly set to 24 HU (note step function-like drop in HU at air/phantom boundary for OBI reconstruction, which is sharper than that of FBCT).

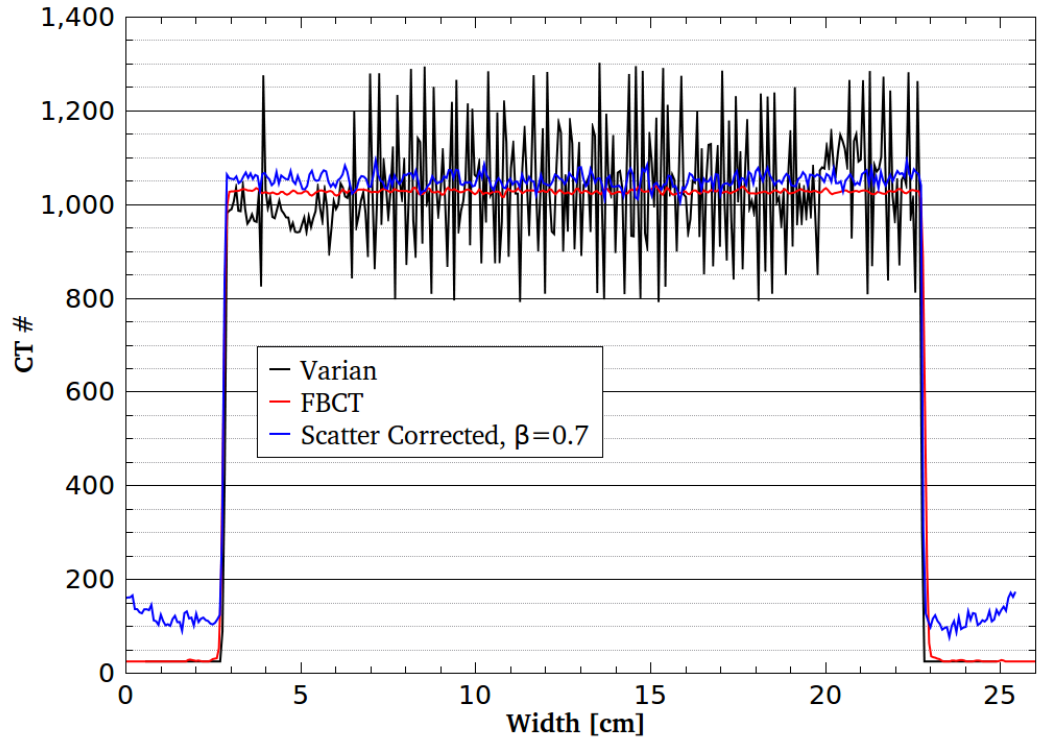

Figure 5.6: Comparison of profiles across the center of a uniform region in the reconstructed ACR accrediation phantom for scatter corrected CBCT data and Varian OBI data.

5.2.2 HU Accuracy

The ACR phantom contains a HU verification module, which includes four embedded test objects of various known materials (bone equivalent material, acrylic, low density polyethylene, and air), shown in Figure 5.7. To study reconstructed HU accuracy, a region of interest (ROI) was selected in each test material. For each ROI, the mean HU and standard deviation from the mean was calculated. The ROI size had an area of about 780 voxels, and care was taken not to place the ROI near the edges of the test objects. The mean HU value for each ROI taken from the CBCT images was then compared with the mean value obtained in the FBCT image, and the absolute HU difference was calculated. Table 5.3 presents the mean reconstructed HU in the four test objects for the raw CBCT, scatter corrected CBCT ($\alpha = 0.2$, $\beta = 0.7$), and Varian OBI reconstructed CBCT images. In the quality assurance program for the OBI, Yoo et al recommend that the reconstructed HU agree to within ± 40 HU of the expected value [67]

In the uncorrected CBCT data, it can be noted that the higher density materials (bone, acrylic, and polyethylene) were all reconstructed with lower HU values than those obtained from the FBCT data, while air was reconstructed with a much larger mean HU. After applying the scatter correction, there is a great improvement in the HU accuracy of the higher density materials, with their difference from the FBCT values agreeing to within one standard deviation. For the air ROI, the scatter correction provides a small improvement (a difference of 247 HU to 190 HU), however it is far from satisfactory. This is most likely a more general problem in reconstructing air from the CBCT data.

For the Varian OBI reconstructed data, the large amount of image noise manifested as large standard deviations on the ROI mean values. In particular, the OBI bone ROI had a standard deviation of 144 HU, compared with 37 HU for the scatter corrected CBCT and 6 HU for the FBCT data. The differences between OBI and FBCT HU values in the higher density materials were also large, ranging from -51 to +212 HU. Where the OBI performed well was in the reconstruction of air, with a difference of

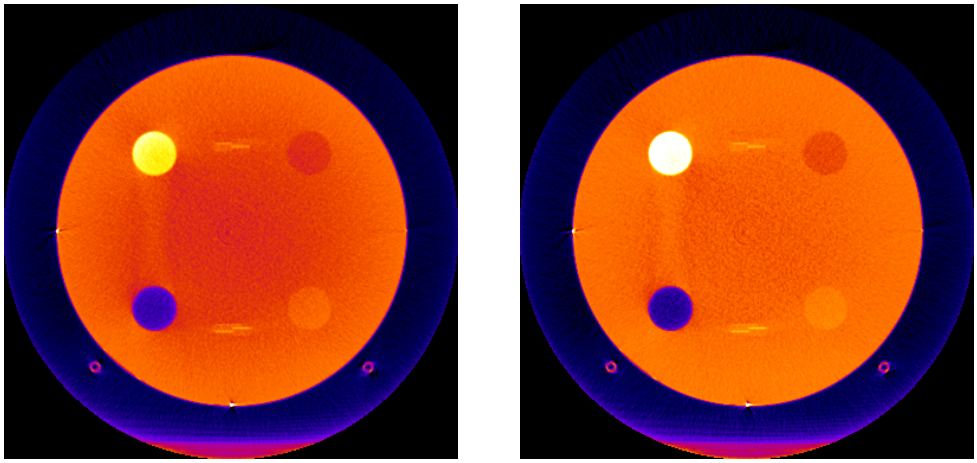

(a) Uncorrected CBCT

(b) Corrected CBCT

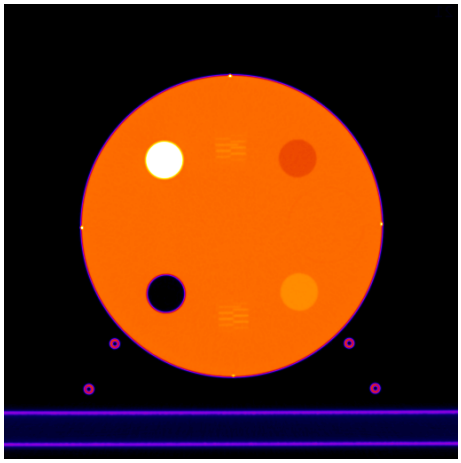

(c) FBCT

Figure 5.7: Reconstructed CBCT slices of the ACR phantom HU verification module for (a) raw (uncorrected) and (b) scatter corrected data. The result from a conventional fan-beam CT scanner is shown in (c). Note the cupping and streaking artifacts in the CBCT images.

only 3 HU from the FBCT result, and a standard deviation similar to that of the scatter corrected CBCT.

The distribution of voxel HU values in each ROI can give some insight into the behaviour of the scatter corrected and OBI CBCT data. Figure 5.8 shows the voxel HU distribution in the bone ROI for the raw, scatter corrected, and OBI CBCT images, as well as the FBCT data. The FBCT values have a narrow, sharply peaked distribution, while the raw and scatter corrected CBCT are much more broadly spread, with a slight skew for larger HU values. The OBI ROI voxels appear to have a tri-modal

Table 5.3: Reconstructed CT numbers for embedded test objects in the ACR phantom for raw CBCT, scatter corrected CBCT, and Varian OBI reconstructed CBCT data, along with absolute difference from the FBCT values. Presented errors are the standard deviation from the mean in the region of interest.

Material	FBCT	Raw CBCT	**Diff.**	Corr. CBCT	**Diff.**	OBI	**Diff.**
Acrylic	1152 ± 4	1021 ± 23	**-131**	1133 ± 25	**-19**	1101 ± 79	**-51**
Polyethylene	936 ± 3	882 ± 18	**-54**	956 ± 20	**+20**	886 ± 31	**-50**
Bone	1864 ± 6	1658 ± 45	**-206**	1899 ± 37	**+35**	2076 ± 144	**+212**
Air	34 ± 3	281 ± 21	**+247**	224 ± 24	**+190**	37 ± 24	**+3**

distribution, with peaks at 1820, 2060, and 2320 HU. This result suggests that the OBI reconstruction software is applying some sort of correction, which in this region is assigning voxels to three different material types. This material assignment correction may also explain why the OBI reconstruction for air agrees well with the FBCT data.

5.2.3 Tuning α and β

The systematic effect of varying the free parameters in the scatter correction (α and β) was investigated. Recall from Eq.(4.9), the parameter α weights the attenuation differences between the MC simulation and measured data, and the anti-scatter grid parameter β weights the simulated scatter air-kerma.

The individual effects of α and β on the scatter correction results were investigated by setting either α or β to a constant value, and varying the second parameter. Figure 5.9 demonstrates the result of fixing $\beta = 0.8$ and varying α, on the scatter corrected profile across a uniform region of the ACR phantom. What can be noticed is that with increasing α, the voxels containing Solid Water experience a slight increase in HU, while air voxels undergo a slight decrease in HU. The HU increase of Solid Water is preferential at the periphery of the phantom, and less pronounced at the center. As well, increasing α also increases the noise of the reconstructed voxels.

These effects can be explained by how α amplifies the differences between the measured and simulated projection pixels. The respective increase/decrease in Solid

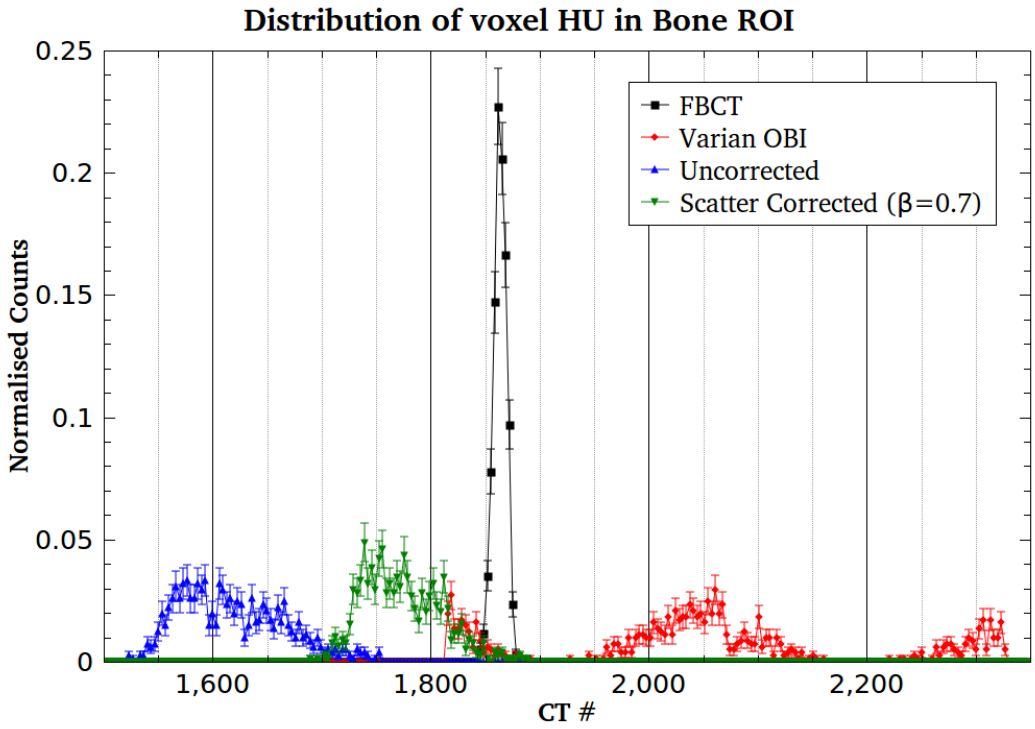

Figure 5.8: Distribution of voxel HU values in the ACR phantom bone ROI.

Water/air HU most likely arises from differences in voxel μ and density after material assignment in the MC simulation. The reappearance of the cupping artifact can also be explained by these differences. Noise is enhanced, since α also amplifies the noise of the measured and simulated projection data.

The effects of setting $\alpha = 0$ and varying β on the uniform region profile are shown in Figure 5.10. As more scatter is accounted for in the correction by increasing β, the cupping artifact is steadily reduced, however the average Solid Water HU value increases beyond that obtained from the FBCT scan. This increase in HU can be understood as the correction subtracting more scatter than is actually present in the measured data, due to the presence of an anti-scatter grid. The Solid Water voxels are then perceived by the reconstruction code as more attenuating than they are in reality.

From the edges of the profile, it would appear that air voxels are relatively insensitive to variations of β. This is not surprising, as the scatter-to-primary ratio in air

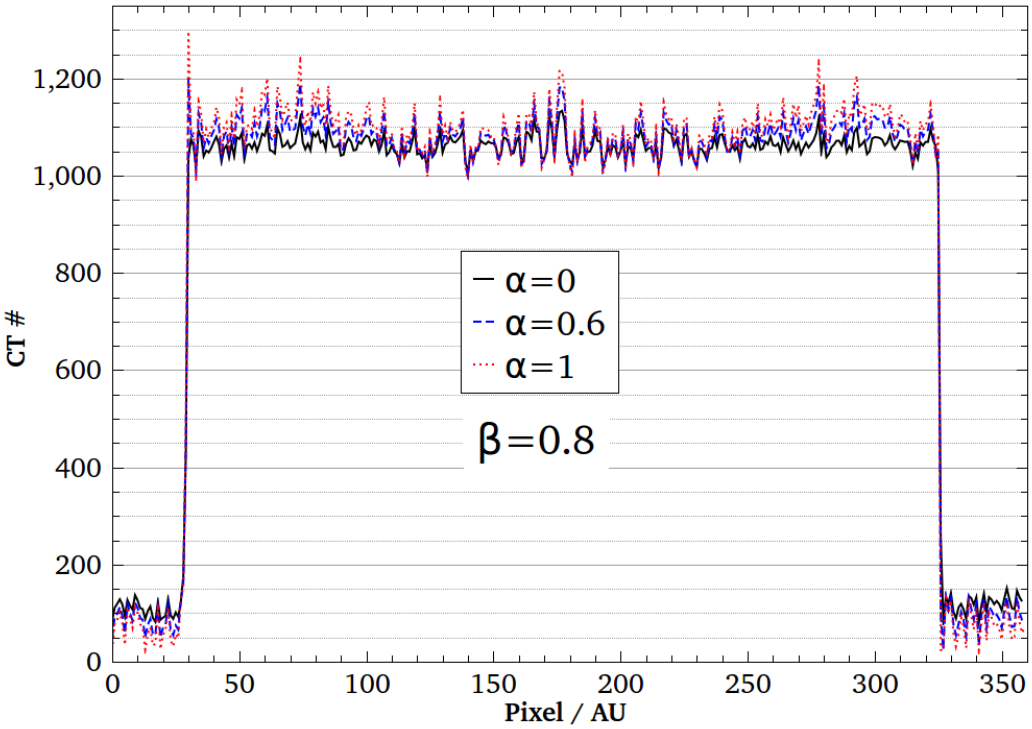

Figure 5.9: Effect of varying α on the scatter corrected profile across a uniform region of the ACR phantom. β was fixed at 0.8.

is expected to be negligible. Variations to the relatively small amount of scattered photons in this region would then be largely unnoticed.

In order to estimate optimum values for α and β, a simple approach based on HU accuracy was followed. Using the procedure outlined in Section 5.2.2, the average HU for material insert ROIs was calculated on scatter corrected images with various α and β values. A cost function, C, was defined as the sum of the squares of differences between the CBCT and FBCT HU values for each material insert (bone, acrylic, polyethylene, and air).

$$C = \sum_{i}^{\text{mat}} (HU_{CBCT} - HU_{FBCT})_i^2 \tag{5.2}$$

The optimum α and β values were then determined as those which minimised C.

This was not a rigorous optimisation procedure, as only a handful of α and β values were investigated. As well, the scatter corrected samples were biased to β values large enough to mitigate cupping artifacts in uniform regions. With these

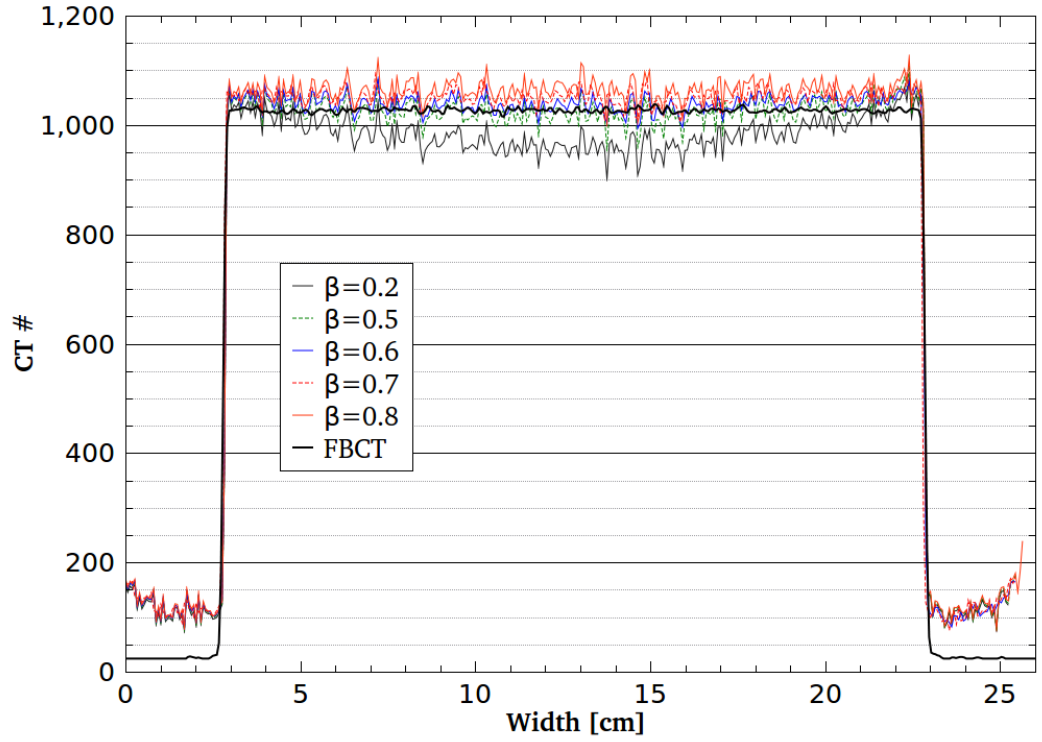

Figure 5.10: Effect of β on the scatter corrected profile across a uniform region of the ACR phantom. α was fixed at 0.

caveats, the optimum values were determined to be $\alpha = 0.1$ and $\beta = 0.8$. It is recommended that a more thorough study of α and β optimisation be investigated in the future.

It remained a question to see how the scatter correction with optimised α and β parameters derived from a cylindrical phantom would perform on a patient scan. To investigate this question, the correction was applied on a scan of an anthropomorphic head phantom, with anatomical geometry.

5.3 RANDO Head Phantom

In the final portion of the study, a RANDO® head phantom (The Phantom Laboratory, Salem, NY), was scanned on CBCT and FBCT. This particular phantom was chosen as it simulates real human tissues and anatomical geometry, testing the clinical relevance of the scatter correction. Following the scatter correction prescription, the

raw CBCT voxels were assigned to anatomical materials and densities according to Table 5.4. The scatter correction, using the "optimum" values of $\alpha = 0.1$ and $\beta = 0.8$ derived from the ACR phantom results, was then applied.

Table 5.4: RANDO head phantom ramp file used for conversion of reconstructed attenuation coefficients to anatomical materials and mass densities.

Material	μ **Range** [$\mathbf{cm^{-1}}$]	ρ [$\mathbf{g/cm^3}$]
Vacuum	[-1.0 : 1.0E-7]	0.0
Air	[1.0E-7 : 0.005]	1.205E-2
Polystyrene Foam	[0.005 : 0.0967]	5.0E-2
Adipose Tissue	[0.0967 : 0.1936]	0.95
Bone Marrow	[0.1936 : 0.205]	1.005
Muscle Tissue	[0.205 : 0.2161]	1.05
Soft Tissue	[0.2161 : 0.2178]	1.05
Skin Tissue	[0.2178 : 0.2244]	1.09
Cartilage	[0.2244 : 0.24]	1.1
Spongiosa	[0.24 : 0.3]	1.18
Cortical Bone	[0.3 : 1.5]	1.92
Steel	[1.5 : 50]	8.06

An example of raw and scatter corrected RANDO CBCT slices, as well as a slice from FBCT, is shown in Figure 5.11. As observed with the ACR phantom study, the CBCT images contain much more noise than the FBCT image. This is in part due to the reduced exposure in CBCT scanning protocols compared to those in FBCT, in order to limit patient dose. Increased noise in CBCT can also be attributed to the poor efficiency of flat-panel detectors compared to the xenon or solid state detectors used in conventional FBCT scanners.

On visual inspection of Figure 5.11a-b, the uncorrected CBCT image exhibits a cupping artifact in the center of the phantom, which the scatter correction helps to reduce. The average HU of the phantom tissue equivalent material and skull appears

to have been increased after correction. This is more readily apparent by looking at a line profile across both the raw and corrected CBCT slices (Figure 5.12). In this profile, the two peaks corresponding to the cranial bone are clearly visible, surrounded by tissue equivalent material. To assess the performance of the scatter correction, a profile across a FBCT slice rigidly registered with the CBCT slices was also measured.

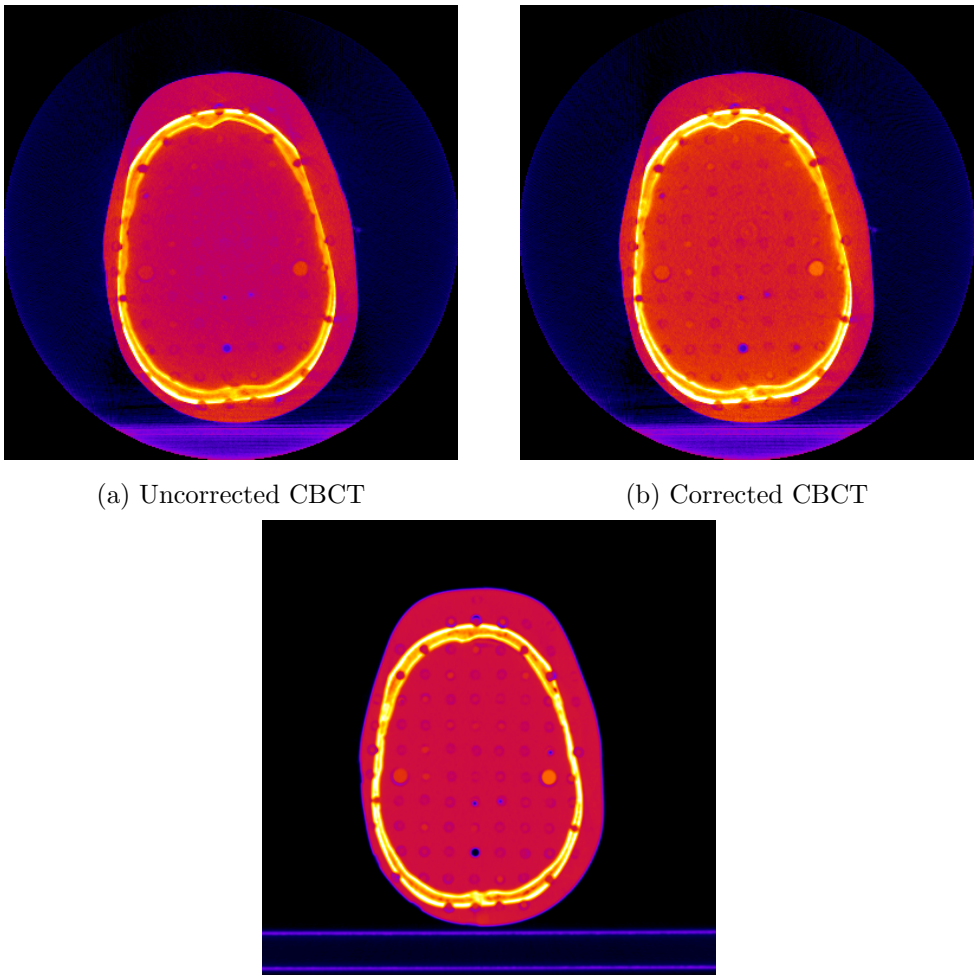

(a) Uncorrected CBCT

(b) Corrected CBCT

(c) FBCT

Figure 5.11: Reconstructed CBCT slices of the RANDO phantom for (a) raw (uncorrected) and (b) scatter corrected data. The result from a conventional fan-beam CT scanner is shown in (c).

In this profile, the cupping artifact and low reconstructed phantom HU from the raw CBCT data is evident. After applying the scatter correction, the cupping artifact is all but eliminated, however the reconstructed HU of the tissue equivalent material is brought greater than the ground truth measured by FBCT (1100 HU vs 1010 HU).

In the cranial bone, the scatter corrected CBCT HU values better agree with those of the FBCT profile than the uncorrected CBCT. Looking at the rightmost bone peak in Figure 5.12, the scatter corrected CBCT scan still underestimates the HU. In the leftmost bone region, both raw and scatter corrected CBCT scans are unable to properly resolve the double peak. As observed in the previous phantom studies, the raw CBCT reconstruction of air voxels continues to overestimate the HU, with little effect from scatter correction. The scatter correction with "optimum" α and β parameters does offer some improvement in the image quality of an anatomical phantom, however it does not match the high quality provided by FBCT.

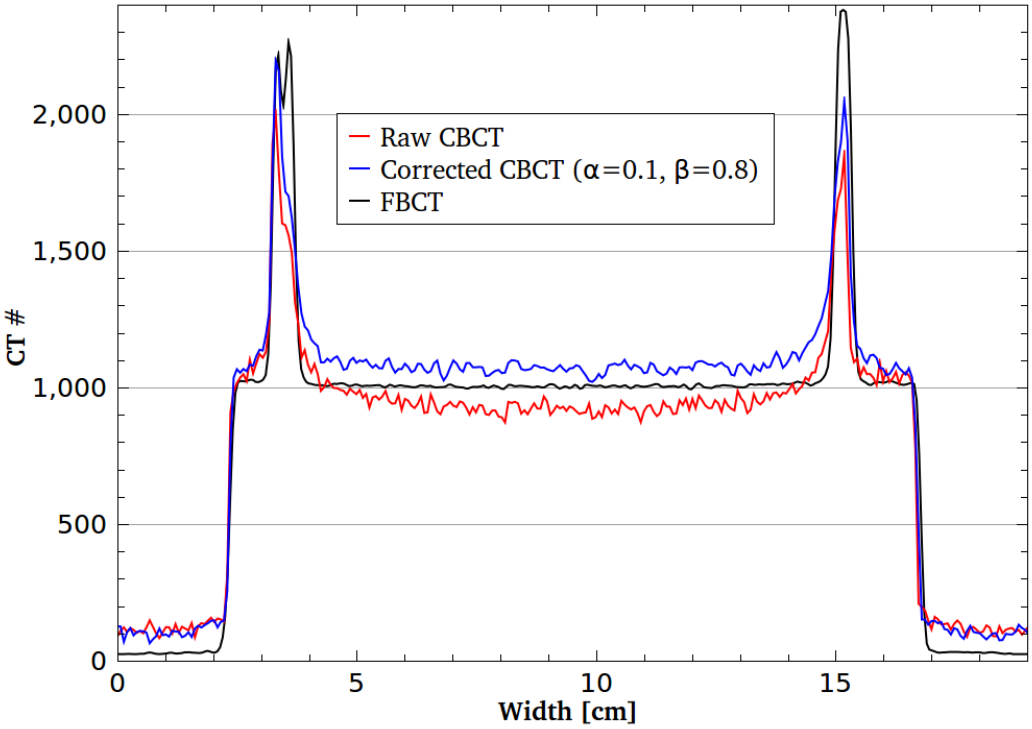

Figure 5.12: Profile across reconstructed RANDO head phantom from raw and scatter corrected CBCT, as well as FBCT.

5.4 Discussion

In practice, the time required to perform the entire scatter correction algorithm (reconstruction, CT-to-density conversion, simulation, correction, reconstruction) as pre-

sented in this work is lengthy. Running the `egs_cbct` projection simulations on a 200 core CPU cluster, and the reconstruction and correction programs on a desktop quad-core CPU, the scatter correction procedure could take up to three hours from start to finish. The bulk of time in this process is spent in the simulation of the 360 projection images. For clinical implementation, this timeframe would ideally be brought down to the order of minutes. Enhancing the efficiency of the simulations may be possible with further implementation of variance reduction techniques, such as position-dependent and region-dependent importance splitting [48]. The smoothness of the scatter distribution could be exploited by using coarser scatter air-kerma scoring, which would decrease simulation time. Scatter smoothness may also be exploited by simulating fewer projection angles and interpolating between them.

Poor HU reconstruction of air was noticed in both raw and scatter corrected CBCT scans, whereas the Varian OBI reconstructed CBCT images had excellent air HU accuracy. This can be attributed to the lack of calibrations and corrections outside of the scatter correction applied to the reconstructed CBCT images used in this work. As listed in Section 3.2.1, the images supplied by the Varian OBI software undergo a number of corrections, notably an HU calibration, which maps the reconstructed voxel attenuation coefficients to known HU values. It would be worth investigating the performance of HU reconstruction accuracy by applying this type of calibration on the raw CBCT data, before applying the proposed scatter correction.

In this work, the scatter suppression effects of the Varian OBI anti-scatter grid were estimated by a simple parameter, β. If the scatter simulation were sufficiently accurate, the anti-scatter grid (and anti-scatter grid parameter) would not be necessary, as all scattered x-rays would be accounted for in the scatter correction. Removal of the anti-scatter grid would also reduce the attenuation of primary photons, allowing for a reduction in patient dose for the same detector exposure. The performance of the scatter correction using a gridless CBCT system was unable to be tested, as the anti-scatter grid is permanently installed on the Varian OBI flat-panel detector.

6

Conclusion

The main objective of this research project was to implement and test the performance of a fast, MC-based scatter correction on CBCT images acquired from a clinical on-board CBCT scanner. An estimate of the scatter and primary x-ray air-kerma contributions at the detector plane was obtained from an MC simulation, using the uncorrected CBCT scan as input. In general, the proposed scatter correction was successful in reducing scatter-based image artifacts. After correction, cupping artifacts in uniform regions were minimised, as well as streaking artifacts between high density objects. The accuracy of HU determination was improved for a range of materials, and in most cases performed better than the commercial software provided by Varian. In an ACR CT Accreditation phantom study, the scatter corrected HU in all material inserts agreed with clinical CT scan data to within 35 HU, with the exception of air. The scatter correction was applied on a scan of an anthropomorphic phantom using parameters optimised from the ACR phantom results, with modest improvement in image quality.

It is recommended that this study be extended to include the application of other CBCT corrections, in particular an HU calibration. These additional corrections should improve the reconstruction accuracy of air voxels, as well as eliminate non-scatter-based artifacts. It would also be valuable to provide a more in-depth model of the CBCT system, such as the x-ray source. In particular, it will be important to account for the bowtie filter and antiscatter grid in the MC simulation, as these are in place during patient scans. A full simulation of the dose deposited in the active layer of the flat-panel detector could test the validity of the assumption of an 'ideal'

detector presented in this work. The time required to run the scatter correction algorithm could be reduced by investigating other variance reduction techniques, and by exploiting the smoothness of the scatter distribution through coarser scatter air-kerma sampling and projection interpolation.

Ultimately, with sufficient image quality, scatter-corrected CBCT images could be used in an adaptive radiotherapy framework. These are promising results towards the reliable use of CBCT images in adaptive treatment replanning.

References

[1] W. H. Organization *et al.*, "Cancer: fact sheet 297," 2012.

[2] C. C. Society, "General cancer statistics." `http://www.cancer.ca/Canada-wide/Aboutcancer/Cancerstatistics/Statsataglance/Generalcancerstats.aspx?sc_lang=en`, 2012.

[3] L. Xing, B. Thorndyke, E. Schreibmann, Y. Yang, T. Li, G. Kim, G. Luxton, A. Koong, *et al.*, "Overview of image-guided radiation therapy," *Medical Dosimetry*, vol. 31, no. 2, pp. 91–112, 2006.

[4] C. Coolens, P. Evans, J. Seco, S. Webb, J. Blackall, E. Rietzel, and G. Chen, "The susceptibility of imrt dose distributions to intrafraction organ motion: an investigation into smoothing filters derived from four dimensional computed tomography data," *Medical physics*, vol. 33, p. 2809, 2006.

[5] L. Dawson and D. Jaffray, "Advances in image-guided radiation therapy," *Journal of clinical oncology*, vol. 25, no. 8, pp. 938–946, 2007.

[6] J. Pouliot, A. Bani-Hashemi, J. Chen, M. Svatos, F. Ghelmansarai, M. Mitschke, M. Aubin, P. Xia, O. Morin, K. Bucci, *et al.*, "Low-dose megavoltage cone-beam ct for radiation therapy," *International Journal of Radiation Oncology* Biology* Physics*, vol. 61, no. 2, pp. 552–560, 2005.

[7] D. Jaffray, D. Drake, M. Moreau, A. Martinez, and J. Wong, "A radiographic and tomographic imaging system integrated into a medical linear accelerator for localization of bone and soft-tissue targets," *International Journal of Radiation Oncology* Biology* Physics*, vol. 45, no. 3, pp. 773–789, 1999.

[8] D. Jaffray, J. Siewerdsen, J. Wong, A. Martinez, *et al.*, "Flat-panel cone-beam computed tomography for image-guided radiation therapy," *International journal of radiation oncology, biology, physics*, vol. 53, no. 5, pp. 1337–1349, 2002.

[9] R. Den, A. Doemer, G. Kubicek, G. Bednarz, J. Galvin, W. Keane, Y. Xiao, and M. Machtay, "Daily image guidance with cone-beam computed tomography for head-and-neck cancer intensity-modulated radiotherapy: a prospective study," *International Journal of Radiation Oncology* Biology* Physics*, vol. 76, no. 5, pp. 1353–1359, 2010.

[10] C. Vargas, D. Yan, L. Kestin, D. Krauss, D. Lockman, D. Brabbins, and A. Martinez, "Phase ii dose escalation study of image-guided adaptive radiotherapy for prostate cancer: Use of dose–volume constraints to achieve rectal isotoxicity," *International Journal of Radiation Oncology* Biology* Physics*, vol. 63, no. 1, pp. 141–149, 2005.

[11] J. Battista, W. Rider, and J. Van Dyk, "Computed tomography for radiotherapy planning," *International Journal of Radiation Oncology* Biology* Physics*, vol. 6, no. 1, pp. 99–107, 1980.

[12] U. Schneider, E. Pedroni, and A. Lomax, "The calibration of ct hounsfield units for radiotherapy treatment planning," *Physics in medicine and biology*, vol. 41, no. 1, p. 111, 1996.

[13] J. J. Sonke, "Cone beam ct guided radiotherapy," *AAPM Summer School Presentation*, 2006.

[14] E. Weiss, J. Wu, W. Sleeman, J. Bryant, P. Mitra, M. Myers, T. Ivanova, N. Mukhopadhyay, V. Ramakrishnan, M. Murphy, *et al.*, "Clinical evaluation of soft tissue organ boundary visualization on cone-beam computed tomographic imaging," *International Journal of Radiation Oncology* Biology* Physics*, vol. 78, no. 3, pp. 929–936, 2010.

[15] G. Ding, D. Duggan, C. Coffey, M. Deeley, D. Hallahan, A. Cmelak, A. Malcolm, *et al.*, "A study on adaptive imrt treatment planning using kv cone-beam ct.," *Radiotherapy and oncology: journal of the European Society for Therapeutic Radiology and Oncology*, vol. 85, no. 1, p. 116, 2007.

[16] S. Yoo, F. Yin, *et al.*, "Dosimetric feasibility of cone-beam ct-based treatment planning compared to ct-based treatment planning.," *International journal of radiation oncology, biology, physics*, vol. 66, no. 5, p. 1553, 2006.

[17] Y. Yang, E. Schreibmann, T. Li, C. Wang, and L. Xing, "Evaluation of on-board kv cone beam ct (cbct)-based dose calculation," *Physics in medicine and biology*, vol. 52, no. 3, p. 685, 2007.

[18] J. Radon, "Über die bestimmung von funktionen durch ihre integralwerte längs gewisser mannigfaltigkeiten," *Berichte über die Verhandlungen der Königlich-Sächsischen Akademie der Wissenschaften zu Leipzig, Mathematisch-Physische Klasse*, vol. 69, pp. 262–277, 1917.

[19] N. E. M. Association, *Digital Imaging and Communications in Medicine (DICOM).* The Association, 1993.

[20] A. Alessio and P. Kinahan, "Pet image reconstruction," *Nuclear Medicine*, vol. 1, 2006.

[21] X. Jia, Y. Lou, R. Li, W. Song, and S. Jiang, "Gpu-based fast cone beam ct reconstruction from undersampled and noisy projection data via total variation.," *Medical physics*, vol. 37, no. 4, p. 1757, 2010.

[22] M. Bazalova, "The use of computed tomography images in monte carlo treatment planning," 2008. PhD Thesis.

[23] C. Constantinou, J. C. Harrington, and L. A. DeWerd, "An electron density calibration phantom for ct-based treatment planning computers," *Medical physics*, vol. 19, p. 325, 1992.

[24] S. Thomas, "Relative electron density calibration of ct scanners for radiotherapy treatment planning.," *British journal of radiology*, vol. 72, no. 860, pp. 781–786, 1999.

[25] N. Strobel, O. Meissner, J. Boese, T. Brunner, B. Heigl, M. Hoheisel, G. Lauritsch, M. Nagel, M. Pfister, E. Rührnschopf, *et al.*, "3d imaging with flat-detector c-arm systems," *Multislice CT*, pp. 33–51, 2009.

[26] J. Barrett and N. Keat, "Artifacts in ct: Recognition and avoidance1," *Radiographics*, vol. 24, no. 6, pp. 1679–1691, 2004.

[27] W. Scarfe and A. Farman, "What is cone-beam ct and how does it work?," *Dental Clinics of North America*, vol. 52, no. 4, pp. 707–730, 2008.

[28] J. Siewerdsen and D. Jaffray, "Cone-beam computed tomography with a flat-panel imager: effects of image lag," *Medical physics*, vol. 26, p. 2635, 1999.

[29] J. Siewerdsen and D. Jaffray, "Cone-beam computed tomography with a flat-panel imager: magnitude and effects of x-ray scatter," *Medical physics*, vol. 28, p. 220, 2001.

[30] J. Bushberg, *The essential physics of medical imaging*. Williams & Wilkins, 2002.

[31] J. Hatton, B. McCurdy, and P. B. Greer, "Cone beam computerized tomography: the effect of calibration of the hounsfield unit number to electron density on dose calculation accuracy for adaptive radiation therapy," *Physics in medicine and biology*, vol. 54, no. 15, p. N329, 2009.

[32] K. Y. Seet, A. Barghi, S. Yartsev, and J. Van Dyk, "The effects of field-of-view and patient size on ct numbers from cone-beam computed tomography," *Physics in medicine and biology*, vol. 54, no. 20, p. 6251, 2009.

[33] J.-P. Bissonnette, D. J. Moseley, and D. A. Jaffray, "A quality assurance program for image quality of cone-beam ct guidance in radiation therapy," *Medical physics*, vol. 35, p. 1807, 2008.

[34] E. Rührnschopf and K. Klingenbeck, "A general framework and review of scatter correction methods in x-ray cone-beam computerized tomography. part 1: Scatter compensation approaches," *Medical physics*, vol. 38, p. 4296, 2011.

[35] E. Rührnschopf and K. Klingenbeck, "A general framework and review of scatter correction methods in cone beam ct. part 2: Scatter estimation approaches," *Medical Physics*, vol. 38, p. 5186, 2011.

[36] J. Persliden and G. Carlsson, "Scatter rejection by air gaps in diagnostic radiology. calculations using a monte carlo collision density method and consideration of molecular interference in coherent scattering," *Physics in medicine and biology*, vol. 42, no. 1, p. 155, 1999.

[37] J. Siewerdsen, D. Moseley, B. Bakhtiar, S. Richard, and D. Jaffray, "The influence of antiscatter grids on soft-tissue detectability in cone-beam computed tomography with flat-panel detectors," *Medical physics*, vol. 31, p. 3506, 2004.

[38] S. Graham, D. Moseley, J. Siewerdsen, and D. Jaffray, "Compensators for dose and scatter management in cone-beam computed tomography," *Medical physics*, vol. 34, p. 2691, 2007.

[39] J. Siewerdsen, M. Daly, B. Bakhtiar, D. Moseley, S. Richard, H. Keller, and D. Jaffray, "A simple, direct method for x-ray scatter estimation and correction in digital radiography and cone-beam ct," *Medical physics*, vol. 33, p. 187, 2006.

[40] R. Ning, X. Tang, and D. Conover, "X-ray scatter correction algorithm for cone beam ct imaging," *Medical physics*, vol. 31, p. 1195, 2004.

[41] L. Zhu, Y. Xie, J. Wang, and L. Xing, "Scatter correction for cone-beam ct in radiation therapy," *Medical physics*, vol. 36, no. 6, p. 2258, 2009.

[42] H. Li, R. Mohan, and X. Zhu, "Scatter kernel estimation with an edge-spread function method for cone-beam computed tomography imaging," *Physics in Medicine and Biology*, vol. 53, p. 6729, 2008.

[43] E. Mainegra-Hing, *Efficient Monte Carlo simulations in kilovoltage x-ray beams*. PhD thesis, Carleton University, 2011.

[44] M. Sun and J. Star-Lack, "Improved scatter correction using adaptive scatter kernel superposition," *Physics in medicine and biology*, vol. 55, no. 22, p. 6695, 2010.

[45] G. Jarry, S. Graham, D. Moseley, D. Jaffray, J. Siewerdsen, and F. Verhaegen, "Characterization of scattered radiation in kv cbct images using monte carlo simulations," *Medical physics*, vol. 33, p. 4320, 2006.

[46] W. Zbijewski and F. Beekman, "Efficient monte carlo based scatter artifact reduction in cone-beam micro-ct," *Medical Imaging, IEEE Transactions on*, vol. 25, no. 7, pp. 817–827, 2006.

[47] G. Poludniowski, P. Evans, V. Hansen, and S. Webb, "An efficient monte carlo-based algorithm for scatter correction in kev cone-beam ct," *Physics in Medicine and Biology*, vol. 54, p. 3847, 2009.

[48] E. Mainegra-Hing and I. Kawrakow, "Variance reduction techniques for fast monte carlo cbct scatter correction calculations," *Physics in medicine and biology*, vol. 55, p. 4495, 2010.

[49] H. Turbell, *Cone-Beam Reconstruction Using Filtered Backprojection*. PhD thesis, Linköpings Universitet, 2001.

[50] L. Feldkamp, L. Davis, and J. Kress, "Practical cone-beam algorithm," *JOSA A*, vol. 1, no. 6, pp. 612–619, 1984.

[51] E. Y. Sidky and X. Pan, "Image reconstruction in circular cone-beam computed tomography by constrained, total-variation minimization," *Physics in Medicine and Biology*, vol. 53, no. 17, p. 4777, 2008.

[52] M. Slaney and A. Kak, "Principles of computerized tomographic imaging," *SIAM, Philadelphia*, 1988.

[53] D. Parker, "Optimal short scan convolution reconstruction for fan beam ct," *Medical Physics*, vol. 9, p. 254, 1982.

[54] N. Metropolis, "The beginning of the monte carlo method," *Los Alamos Science*, vol. 15, no. 584, pp. 125–130, 1987.

[55] I. Lux and L. Koblinger, *Monte Carlo particle transport methods: neutron and photon calculations*, vol. 102. CRC press, 1991.

[56] I. Kawrakow and D. Rogers, "The egsnrc code system: Monte carlo simulation of electron and photon transport (pirs-701)," *National Research Council (NRC) Report*, 2006.

[57] W. Nelson, H. Hirayama, and D. Rogers, "Egs4 code system," tech. rep., Stanford Linear Accelerator Center, Menlo Park, CA (USA), 1985.

[58] W. Nelson, "Pegs4 user manual. slac-265-appendix 3," 1985.

[59] V. M. Systems, *On-Board Imager Physicist Operations.* Varian Medical Systems, 2008.

[60] E. Mainegra-Hing and I. Kawrakow, "Fast monte carlo calculation of scatter corrections for cbct images," in *Journal of Physics: Conference Series*, vol. 102, p. 012017, IOP Publishing, 2008.

[61] L. Dagum and R. Menon, "Openmp: an industry standard api for shared-memory programming," *Computational Science & Engineering, IEEE*, vol. 5, no. 1, pp. 46–55, 1998.

[62] I. Kawrakow, E. Mainegra-Hing, F. Tessier, and B. Walters, "Egsnrc c++ class library," *NRCC Report No. PIRS-898 (Ottawa, Canada, 2005)*, 2005.

[63] E. Mainegra-Hing and I. Kawrakow, "Efficient x-ray tube simulations," *Medical physics*, vol. 33, p. 2683, 2006.

[64] M. Berger, J. Hubbell, S. Seltzer, J. Chang, J. Coursey, R. Sukumar, and D. Zucker, "Xcom: Photon cross sections database," *NIST Standard Reference Database*, vol. 8, pp. 87–3597, 1998.

[65] I. Kawrakow, "On the de-noising of monte carlo calculated dose distributions," *Physics in medicine and biology*, vol. 47, p. 3087, 2002.

[66] G. Ding, D. Duggan, and C. Coffey, "Characteristics of kilovoltage x-ray beams used for cone-beam computed tomography in radiation therapy," *Physics in Medicine and Biology*, vol. 52, p. 1595, 2007.

[67] S. Yoo, G.-Y. Kim, R. Hammoud, E. Elder, T. Pawlicki, H. Guan, T. Fox, G. Luxton, F.-F. Yin, and P. Munro, "A quality assurance program for the on-board imager," *Medical Physics*, vol. 33, no. 11, pp. 4431–4447, 2006.

Appendix A: Convolution Function

A memory-efficient 1D convolution function was written for use in the FDK algorithm. Here, a kernel `g[i]` is convolved with the function data `f[i]`. Generic convolution functions will zero-pad `f[i]`, doubling the amount of data to be stored in memory. In the case of convolving CBCT projection data, this could mean requiring over 2 Gb of available RAM, in addition to other data stored in memory. To conserve memory, a 1D convolution function was written which does not require zero-padding. This is possible by using an if statement which only computes the non-zero components of the convolution sum. This function was written in C.

```
/* 1D convolution that DOES NOT require zero padding (gotta save that memory)
   Written by Pete Watson, Nov 2011
*/
void conv1d(float *f, float *fg, int fsz, float *g, int gsz){
  int i,j;
  int gmid = gsz/2;
  double dtmp;
  for (i=0; i<fsz; i++){
    dtmp=0;
    for (j=-gmid; j<gmid; j++){
      if((i-j)>0 && (i-j-1)<fsz){
        dtmp += (double)g[j+gmid]*f[i-j-1];
      }
    }
    fg[i]=dtmp;
 }}
```